Broadband Ocean Bottom Seismometer Noise Properties

Helen A. Janiszewski*[1], Z. Eilon[2], J.B. Russell[3], B. Brunsvik[2], J.B. Gaherty[4], S.G. Mosher[5], W.B. Hawley[6], and S. Coats[1]

1. Department of Earth Sciences, University of Hawaiʻi at Mānoa, Honolulu, HI
2. Dept. of Earth Science, University of California, Santa Barbara, CA
3. Dept. of Earth, Environmental and Planetary Sciences, Brown University, Providence, RI
4. School of Earth & Sustainability, Northern Arizona University, Flagstaff, AZ
5. Department of Earth and Environmental Sciences, University of Ottawa, Ottawa, Canada
6. Lamont-Doherty Earth Observatory of Columbia University, Palisades, NY

Abbreviated Title: BBOBS Noise Properties

* Corresponding author: hajanisz@hawaii.edu, 1-808-956-0313

Summary

We present a new compilation and analysis of broadband ocean bottom seismometer noise properties from 15 years of seismic deployments. We compile a comprehensive dataset of representative four-component (seismometer and pressure gauge) noise spectra and cross-spectral properties (coherence, phase, and admittance) for 551 unique stations spanning 18 US-led experiments. This is matched with a comprehensive compilation of metadata parameters related to instrumentation and environmental properties for each station. We systematically investigate the similarity of noise spectra by grouping them according to these metadata parameters to determine which factors are the most important in determining noise characteristics. We find evidence for improvements in similarity of noise properties when grouped across parameters, with groupings by seismometer type and deployment water depth yielding the most significant and interpretable results. Instrument design, that is the entire deployed package, also plays an important role, although it strongly covaries with seismometer and water depth. We assess the presence of traditional sources of tilt, compliance, and microseismic noise to characterize their relative role across a variety of commonly used seismic frequency bands. We find that the presence of tilt noise is primarily dependent on the type of seismometer used (covariant with a particular subset of instrument design), that compliance noise follows anticipated relationships with water depth, and that shallow, oceanic shelf environments have systematically different microseism noise properties (which are, in turn, different from instruments deployed in shallow lake environments). These observations have important implications for the viability of commonly used seismic analysis techniques. Finally, we compare spectra and coherences before and after vertical channel tilt and compliance noise removal to evaluate the efficacy and limitations of these now standard processing techniques. These findings may assist in future experiment planning and instrument development, and our newly compiled noise dataset serves as a building block for more targeted future investigations by the marine seismology community.

Key Words

Seismic noise; Seismic instruments; Instrumental noise; Site effects; Pacific Ocean; Atlantic Ocean

1. Introduction

Over recent decades, the marine seismological community has made steady progress in the deployment of increasingly high-quality and large(r)-N broadband ocean-bottom seismometer (BBOBS) networks. It is approximately 30 years since the advent of modern-standard ocean-floor seismic instruments (Cox, et al., 1984; Montagner et al., 1994; Webb et al., 1994; Purdy & Orcutt, 1995; Collins et al., 2001; Stephen et al., 2003) led to the formation of the Ocean Bottom Seismic Instrument Pool (OBSIP) in 1999 (Aderhold et al., 2019). It is approximately 10 years since the conception and execution of one of the most ambitious community BBOBS deployments to date: the Cascadia Initiative (Toomey et al., 2014). Systematic archiving of seismic and pressure-gauge data at the Incorporated Research Institutions for Seismology (IRIS) Data Management Center (DMC), along with community tools for preprocessing BBOBS data (*e.g.*, ATaCR, Janiszewski et al., 2019; DLOPy, Doran & Laske, 2017) have substantially expanded the reach and salience of BBOBS data across the wider seismological community. With the recent reorganization of the national US instrument pool into the Ocean Bottom Seismic Instrument Center (OBSIC), the emergence of improving hardware, renewed planning towards long-term BBOBS observatories (Kohler et al., 2020), and the evolution of new seafloor technologies (Spica et al., 2020; Lior et al., 2021), this is an apposite juncture to assess the systematics of BBOBS noise traits.

Analyses of spectra (including both seismometer and pressure-gauge data) for individual deployments suggest significant seismic noise variations exist among deployed BBOBSs (Yang et al., 2012; Sumy et al., 2015; Barcheck et al., 2020; An, 2021). Direct comparisons of their noise have largely focused on single-instrument tests rather than arrays (Webb, 1998), or pilot studies that contrast different installation techniques (*e.g.*, Collins et al., 2001). These are limited in location and do not include all types of BBOBS design in the modern OBSIC fleet. To date, a systematic noise comparison across deployments that encompasses the full range of instrument designs, water depths, and site conditions does not exist. Recent analyses using the Cascadia Initiative dataset demonstrate variability as a function of instrument design and water depth (Bell et al., 2015; Hilmo & Wilcock, 2020), motivating expansion of such analyses across deployments.

In this study, we present a comprehensive dataset describing the last 15 years of US-funded BBOBS array deployments (Figure 1). We compute representative multi-component noise spectra from stations deployed in a variety of environments, water depths, and using several different instrument designs. We calculate cross-channel coherences, upper and lower bounds on typical noise, and investigate systematics of noise within a variety of frequency bands spanning from 0.001 to 1 Hz. Using this dataset, we offer a comprehensive and quantitative review of the character and sources of noise on BBOBS instruments.

2. Background

2.1 Noise Sources

The noise power spectrum from 0.001–1 Hz on BBOBS instruments is influenced by the presence and strength of microseism noise, infragravity waves, and tilt or bottom current noise, as well as complications due to instrument response and shear-mode wave propagation at higher frequencies (Figure 2). Microseism noise is the broad, high-amplitude peak between 0.5-0.05 Hz that dominates the ambient seismic energy field world-wide (Peterson, 1993; McNamara & Buland, 2004). Its prevalence has resulted in the traditional distinction between "high frequency" (> 1 Hz) and "low frequency" (< 0.05 Hz) low-noise observational seismic bands. To first order, seafloor observations of microseismic noise are consistent with the long history of observations on land. The noise spectrum in this band is typically divided into two peaks - the secondary microseism, with multiple sub-peaks at frequencies within 0.1 - 0.5 Hz (Stephen et al., 2003) and a dominant peak located at ~0.14 Hz, and the primary microseism, which peaks at ~0.07 Hz (Webb, 1998).

Acoustic waves produced by the interaction of wind-generated ocean waves with the seafloor constitute the secondary microseism (Longuet-Higgins, 1950). Several dominant mechanisms generate these interacting waves, including storm-generated swell, coastline reflected waves, and interactions of waves generated by multiple storms (Bromirski et al., 2005; Ardhuin et al., 2011).

Broadly, the amplitudes of higher frequency energy within the secondary microseism correlate with the local sea state, while waves generated from distant storms and their coastal reflections play a more important role at longer periods within this band (Babcock et al., 1994; Stephen et al., 2003; Bromirski et al., 2005). These properties can lead to systematic differences between ocean basins. The Pacific Ocean appears to propagate energy from larger, more distant storms with higher sustained wind speeds, leading to a secondary microseism peak that extends to lower frequencies than in the North Atlantic Ocean (Babcock et al., 1994; Webb, 1998), although only limited numbers of instruments were used for these early measurements. More recently, Yang et al. (2012) observed systematic differences in long period microseismic energy between BBOBSs deployed in the South Pacific and the Tasman Sea off opposite coasts of New Zealand, with instruments in the marginal sea relatively deficient in longer period energy. Additionally, the secondary microseism peak may shift to higher frequencies in lake environments (Xu et al., 2017; Smalls et al., 2019).

The primary microseism peak is generated by direct interaction (shoaling) of ocean waves with the shoreline and rough seafloor topography (Hasselmann, 1963; Ardhuin, 2018). In the deep ocean, the primary microseism peak is weaker than the secondary microseism (Ardhuin et al., 2015). At longer periods than the primary microseism is a noise spectral-amplitude minimum termed the "noise notch" (Webb, 1998). Significant differences exist in the microseism properties between deep and shallow water; in shallow water, the primary microseism has higher amplitudes than the secondary microseism due to the direct coupling between the ocean swell with the seafloor (Webb & Crawford, 2010; Hilmo & Wilcock, 2020). This also reduces or removes the noise notch at shallow BBOBS (Hilmo & Wilcock, 2020).

At lower frequencies still, noise from infragravity-waves and bottom-currents is prevalent in BBOBS data. These signals are largely absent or strongly diminished at onshore sites. Infragravity waves are long period (< ~ 0.03 Hz) ocean waves generated in coastal regions. Typically, these have maximum amplitudes along the continental shelves, but a small amount of infragravity wave energy may reach and subsequently propagate efficiently across the open ocean (Webb et al., 1991; Uchiyama & McWilliams, 2008; Ardhuin et al., 2014). Propagation into the deep ocean depends on coastal morphology (Aucan & Ardhuin, 2013; Crawford et al., 2015; Bogiatzis et al., 2020). Infragravity waves in the deep ocean perturb the seafloor at long (> 40 km) wavelength, such that coherent signals are observed on the seismic and pressure channels of BBOBSs (Crawford et al., 1991). On the seismometers, this compliance noise is strongest on the vertical component. Compliance noise also affects horizontal components, but is typically obscured by other noise sources, chiefly the effects of seafloor currents (Webb et al., 1991; Doran & Laske, 2016). The pressure perturbations associated with infragravity waves have a frequency-dependent decay with depth in the water column. As a result, the maximum frequency at which seafloor compliance affects BBOBSs decreases in deeper water (Crawford & Webb, 2000; Bell et al., 2015), and the minimum frequency extends beyond the low-frequency end of the sensitivity of modern instruments (Figure 2).

Bottom-current noise is a consequence of seafloor currents directly buffeting the instrument (Webb, 1998; Collins et al., 2001). It affects the entire seismic band (Webb, 1998), but is strongest at frequencies < 0.1 Hz, and leads to substantially higher noise levels on the horizontal components. In the case that the sensor is not perfectly level, this bottom-current noise can also couple into the vertical component, resulting in tilt noise (Crawford & Webb, 2000). These follow a power-law increase with decreasing frequency. Current noise is analogous to wind-driven noise in land stations, but generally much stronger. On horizontal components, this noise largely eliminates the traditional low-noise observational band at frequencies below the microseism; analyses of earthquake signals on these components are generally limited to high-amplitude recordings (*i.e.*, large magnitude and/or nearby events).

2.2 Noise Corrections

Tilt and compliance noise imply predictable relationships between the vertical and horizontal, and vertical and pressure time series, respectively, at an individual BBOBS. Transfer functions quantify the admittance, coherence, and phase relationships (in frequency space) between these components (see Crawford & Webb, 2000; Bell et al., 2015). Vertical seismic components can be corrected for tilt and compliance noise using the appropriate transfer functions (Crawford & Webb, 2000), leading to a reduction of noise levels on this component. The approach relies on the statistical property of signal stationarity: temporally consistent transfer functions can be obtained by averaging frequency-domain relationships between components across multiple time windows. Typical approaches for calculating transfer functions include averaging over long time periods, such that transient signals occupy a relatively small percentage of time windows (Yang et al., 2012), or removing transient signals prior to processing (Bell et al. 2015; Janiszewski et al., 2019).

Seafloor compliance is theoretically a time-invariant property describing the response of the local subsurface to infragravity waves, and its admittance spectrum can be inverted for shallow shear velocity structure (*e.g.*, Crawford et al., 1991; Ruan et al., 2014; Doran & Laske, 2019; Mosher et al., 2021). This implies that an effective compliance correction can be obtained from a small number of time-averaged transfer functions. However, tilt can vary with time, as instruments settle in soft sediment and the degree and azimuth of non-verticality change. Some instruments also perform gyroscopic re-leveling cycles, with varying periodicity (Bell et al., 2015). To address these issues, tilt corrections derived from shorter-duration (*e.g.*, daily) transfer functions may prove more effective (*e.g.*, Bell et al., 2015).

3. Methods

3.1 Inclusion Criteria

Our study includes BBOBSs deployed as part of experiments facilitated by OBSIP or OBSIC from 2005 to the present. Each BBOBS in our dataset satisfies the following criteria. (1) It contains a 3-component, wideband or broadband seismometer (*i.e.*, with flat instrument response between ~0.01 and ~10 Hz). We restrict our analysis to BBOBS designs with seismometers that are still actively used in the OBSIC fleet, which includes Guralp CMG-3T (CMG-3T), Nanometrics Trillium Compact (T-Compact), and Nanometrics Trillium 240 (T-240) instruments. (2) It includes a wide-band pressure sensor: either a differential pressure gauge (DPG) or an absolute pressure gauge (APG). (3) All four components of the BBOBS recorded data at a sample rate of at least 5 samples-per-second (sps). Our study does not constitute a quantification of overall data quality; we do not account for station dropouts, broken channels, or instrument return rate. We focus on data that are considered “good” to offer an analysis of noise properties that are representative of normal BBOBS operations.

3.2 Data Selection and Processing

To investigate the relationship of the noise characteristics of BBOBSs with deployment and instrument properties, we select a subset of data at each station from which to calculate power spectra, cross-component coherence, admittance, and phase spectra, which make up the transfer functions used for noise corrections (Bell et al., 2015; Crawford & Webb, 2000). We examine 25 days of data that are not significantly contaminated by earthquake signals, instrument glitches, or other transient signals at each BBOBS using the ATaCR code package (Janiszewski et al., 2019). These days are randomly distributed throughout each deployment to average across any long term drift, instrument releveling, or seasonal variability (Bell et al., 2015; Stähler et al., 2016). For all seismometer and DPG channels, we remove the instrument response using a high pass filter with a corner frequency of 1000 s. The response is not removed from APG channels, but we filter the data using the same procedure. All data are downsampled to 5 sps using an anti-alias filter with a corner frequency of 1.25 Hz.

We window each day of data into sixteen, 7200-second segments, overlapping by 30%, and apply a flat-Hanning taper to the windows. We calculate the auto- and cross-power spectral density functions from the finite Fourier transforms of the time series (Bell et al., 2015; Bendat & Piersol, 2010) for each of the 16 windows. Any windows that contain transient signals identified via quality control procedures (see Janiszewski et al., 2019 for details) are discarded; if more than 6 windows are discarded, the entire day is rejected and not counted towards the 25-day sample. The windows are subsequently averaged to calculate spectral density functions for each day of data.

We then calculate deployment-average spectral functions for each station by averaging over all windows. A second quality-control step discards individual days that significantly (at 95% confidence level) increase the standard deviation of the noise properties (Janiszewski et al., 2019). This avoids the inclusion of days that are dominated by anomalous signals unrepresentative of normal station noise. While this processing procedure may not capture the full range of variability and discards malfunctioning data segments, it is appropriate for examining systematic trends at functioning BBOBSs. For analysis and comparison, we take full-octave averages of the spectra in $\frac{1}{8}$ octave intervals following the procedure of McNamara & Buland (2004). We visually inspect all averaged spectra and discard any that contain data dropouts, flatlined or obviously non-functioning instruments, or instruments where the secondary microseism peak was not visible *(e.g.*, anomalously high noise floor). This results in average spectra for vertical (*Z*), horizontal (*H1, H2,* or collectively *H*), and pressure (*P*) components at each BBOBS, as well as average cross-component coherence, admittance, and phase functions.

Lastly, we use the computed transfer functions to estimate average tilt- and compliance-corrected *Z* spectra for each BBOBS (Crawford & Webb, 2000). In our discussion, we use *Z-corrected* to refer to the *Z* component where both tilt and compliance noise have been removed. To compute the *Z-corrected* spectra, all four components of a BBOBS must pass the aforementioned quality control procedures. After quality controls, we are left with data from 551 BBOBS with waveforms archived in the IRIS DMC that had at least one component, and 404 that have all four components. This includes instruments from 18 seismic experiments, with deployment years ranging from 2005 – 2019 (Table S1). In calculating the transfer functions, we also calculate the cross spectral properties: the coherence, admittance, and phase (Bell et al., 2015). Of these, coherence is the simplest to interpret since it varies between zero and one and does not reflect discrepancies in instrument gain or polarity. High coherence between the vertical and pressure components at long periods indicates the presence of compliance noise, and high coherence between the vertical and horizontal components indicates tilt noise (Crawford & Webb, 2000). High vertical-pressure coherence also occurs within the microseism band, particularly near the secondary microseism. We analyze the coherences in order to constrain variability in the properties of tilt and compliance noise on the BBOBS.

The approach of Crawford & Webb (2000) scales the transfer function with the coherence; that is, a larger noise removal in the data will occur in locations with higher coherence values. Traditionally, tilt- and compliance- corrections are only calculated at frequencies < 0.1 Hz; another approach is to only calculate corrections in frequency ranges where the coherence between components is above a cutoff value (Bell et al., 2015; Tian & Ritzwoller, 2017). High coherences are also often observed in the secondary microseism band, and this transfer function correction approach has been extended to these higher frequencies with success (*e.g.*, Bowden et al., 2016). Since our investigations only rely on a systematic estimate of noise reduction after corrections, we calculate the corrections following Crawford & Webb (2000) across the entire frequency band, rather than exclude lower-coherence frequency ranges altogether. This may lead to a slightly higher estimate of noise reduction at frequencies with low coherence, but the effect should be minimal. In addition, users of BBOBS data should be cautious of potential distortion of time series or amplitude errors when applying corrections systematically over the entire frequency band. A more targeted removal approach may be required for some use cases.

3.3 Metadata Compilation

To compare the noise with instrument and deployment properties, we compile metadata information for all stations in our dataset. Instrument design was obtained from the IRIS DMC, and verified through review of individual cruise reports. Instruments are designed by one of the three centers that comprised OBSIP – the Lamont Doherty Earth Observatory (LDEO), Scripps Institute of Oceanography (SIO), and Woods Hole Oceanographic Institution (WHOI). We classify each instrument among eight unique designs according to differences in the seismometer, pressure gauge, or the overall package in which the instruments are housed. We do not attempt to distinguish between upgrades in datalogger versions within a given instrument design. For all designs, we utilize the instrument responses archived with the data at the IRIS DMC. Our categorizations mirror those given in the OBSIP Final Report (Aderhold et al, 2019); however, we additionally distinguish between LDEO broadband instruments that were deployed with either a DPG or an APG. We also include information about the geographic environment of the instruments, which includes ocean basins and marginal seas as defined by the International Hydrographic Organization (1953). The deployments were predominantly located in the Pacific Ocean and its marginal seas, but also include the Atlantic Ocean and Lake Malawi. Details for our instrument design categorization are given in Table 1, and the frequency distributions of these parameters are shown in Figure S1. We also record the experiment in which each BBOBS was deployed.

We query the water depth of each station from the IRIS DMC; these values are reported by cruise logs, typically from sonar readings at the deployment location or through acoustic ranging (Russell et al., 2019), and are typically accurate to ~10m. Where possible, we determine the following geographic properties for each instrument using global compilations: the distance to the nearest land, the distance to the nearest tectonic plate boundary, the age of the underlying oceanic crust, the sediment thickness beneath each BBOBS, and the mean annual surface current velocity. To determine the distance to coastline, we calculate the distance to the nearest major landmass from each station using the dataset of Lee et al. (2018). This parameterization ignores small islands, as we are most interested in the relationship between noise sources that may arise from ocean-shelf interactions. We calculate the distance to the nearest plate boundary using the compilation of Bird (2003).

We estimate crustal age using the 2-arc-minute resolution seafloor age map from Müller et al. (2008), which is primarily constrained by prominent marine magnetic anomalies. We use the GlobSed model (Straume et al., 2019), a 5-arc-minute total sediment thickness grid for the world's oceans and marginal seas, to estimate sediment thickness. We compute mean annual surface current velocity estimates using the near-surface velocity climatology data from the Global Drifter Program (Laurindo et al., 2017). For all three datasets, we estimate the variable at the BBOBS by extracting the geographic grid point that overlaps with the site location. If this did not exist, no value was assigned. In total, we compile and examine 11 metadata parameters at each BBOBS: *"Experiment", "Instrument Design", "Seismometer", "Pressure Gauge", "Environment", "Water Depth", "Distance from Land", "Distance to Plate Boundary", "Surface Current", "Sediment Thickness",* and *"Crustal Age"* (Table S2). The distributions for these parameters are shown in Figure S2.

There are limitations to our sampling of metadata in this analysis. Many investigated parameters are not evenly distributed. For example, the maximum value for distance to the coastline is 4020 km, but > 75% of stations have values less than 1000 km. Some parameters do not have available values for all stations. For example, oceanic crustal age estimates do not exist for stations located on the continental shelves, on submerged Zealandia continental crust, and for lacustrine stations.

3.4 Spectral Angle Calculation and Analysis

A primary goal of this study is to determine the properties (*i.e.*, metadata) of a BBOBS that determine its noise characteristics. To this end, we divide the dataset of station spectra into subgroups defined by metadata parameter(s), and then quantify the similarity of spectra within each subgroup. If a certain parameter is highly determinative of noise, then spectra within each subgroup defined by that parameter should be similar to each other, but quite distinct from spectra in the other subgroups.

We use the "spectral angle" to quantify the (dis)similarity of spectra. This metric accounts for differences in the shape, but not absolute amplitudes, of stations' spectra (*e.g.*, Sohn & Rebello, 2002; Wan et al., 2002). We are primarily interested in variations in sources of noise (*e.g.,* changes in the frequency distribution and extrema of different noise peaks and troughs), and not in an average noise-level metric. The spectral angle is better suited to this than other metrics we tested (*e.g.,* the Euclidean distance) that are overly sensitive to absolute amplitude. Spectral angle is also diagnostic of differences in noise floor between instruments, due to differences in curvature of the spectra between high noise peaks.

For a given pair of spectra, s_i and s_j, the spectral angle is computed in log-frequency space as

$$\theta_{i,j} = \cos^{-1}\left(\frac{s_i \cdot s_j}{|s_i||s_j|}\right), \tag{1}$$

We assign a penalty to each individual spectrum, defined as the root-mean-square of its spectral angle with all other spectra in its subgroup:

$$p_i = \sqrt{\frac{1}{n-1}\sum_{j\neq i} {\theta_{i,j}}^2}. \tag{2}$$

where n is the number of spectra in the subgroup. We then calculate the summed penalty for each subgroup, describing mean spectral similarity, as the sum of the individual stations' penalties:

$$P = \sum_{i}^{n} p_i. \tag{3}$$

Finally, the overall penalty function for a given subgrouping scheme is the sum across all subgroups' penalties.

Since the effect of noise is expected to differ between the *Z*, *H1* and *H2*, and *Z-corrected* components, we examine each of these independently. For consistency, we only analyze the 404 instruments with four components that passed quality control. Since the BBOBSs are randomly oriented on the seafloor, we treat the *H1* and *H2* components as two representations of the horizontal noise, giving 808 spectra for this *H* component.

To start, we calculate three total penalties for the entire group of BBOBSs described above (for *Z, Z-corrected,* and *H* components). This yields a baseline measure of spectral dissimilarity amongst all stations in the dataset. We then systematically divide the dataset into subgroups of stations defined by each metadata parameter. For example, we use the "seismometer" metadata parameter to construct three subgroups of noise spectra defined by the parameter's three categorical subdivisions: T-240s, CMG-3Ts, and T-Compacts. We calculate a penalty for each of the *k* subgroups, Pk, as above, and a total penalty, *P*, as the summation of the three subgroup penalties. This is done for each seismic component *Z, H*, and *Z-corrected*, in turn. In general, *N* in each subgroup varies with our choice of metadata parameter, as discussed below. Subgroups with zero or one station are excluded from the penalty calculation. The larger the reduction in overall penalty function when stations are subdivided according to a given metadata parameter, the more closely linked that parameter is to noise spectral shape.

The metadata parameters we use to subdivide the spectra fall into one of three types: (1) categorical, (2) numerical, (3) incomplete-numerical. For categorical parameters, we use one subgroup for each category. For numerical parameters, we utilize two subgroups, separated by a cutoff value. We determine the optimal threshold value by grid searching to obtain the cutoff that yields the two most internally similar subgroups. Finally, for the numerical variables that lack some data entries *(i.e.*, semi-numerical; Figure S2b, d,f), we place stations lacking numerical values into a separate subgroup, and use the grid-search approach for numerical parameters for the remaining stations, yielding three subgroups.

Since multiple parameters influence the noise spectra, the subgrouping scheme uses a hierarchical framework. First, we perform the above analysis for each individual metadata parameter. We refer to such single-parameter subgroups as a “1-layer” analysis. For parameters that result in relatively high levels of penalty reduction, we then test the effect of producing additional subgroups by repeating this procedure two times, resulting in a “3-layer” analysis. In all cases, we evaluate success by computing the penalty reduction value, which compares the summed penalty to the baseline penalty.

4. Results

4.1 Average Noise Spectra

We present average power spectra for each BBOBS seismometer component in Figure 3. The *Z* component data are, on average, between the New High and Low Noise Model (NHNM and NLNM; Peterson, 1993). As expected, the *H* components have higher values, above or near the NHNM at all frequencies. At frequencies lower than ~ 0.1 Hz, the *H* components are on average ~20 - 35 dB noisier than the vertical components, likely due to bottom-current noise (Webb, 1998). The difference between components is less pronounced at shorter periods. Both the secondary and primary microseism are observed as clear peaks at ~ 0.14 and ~0.07 Hz, respectively, where the secondary peak is on average higher than the primary. However, the greatest variability between the spectra is observed in the primary microseism band on both the *Z* and *H* components. At frequencies < 0.05 Hz, the infragravity signal manifests as an additional peak on a subset of the vertical spectra. This peak is not observed on the horizontal components since it is drowned out by the stronger bottom-current noise. We also examined the pressure spectra; however, significant variability between experiments suggests a possible instrumentation or gain error for subsets of BBOBSs. Pressure gauge response functions can be prone to calibration error, although the cited variability is typically less than the order of magnitude observed here (Yang et al., 2012; Doran et al., 2019). At least one of the apparently anomalous pressure spectra is related to an error in the AACSE data that has since been reported and resolved in the IRIS DMC (Figure S5, S6). We note, however, that gain errors do not affect our ability to perform compliance removal, or interpret coherence or phase information between the *Z* and *P* components.

As predicted, for the *Z-corrected* components, we observe a reduction in noise across all frequencies after the transfer function corrections were applied. On average, the corrected spectra are ~ 5-10 dB quieter than the original, but reductions as large as ~ 40 dB are observed. Maximal noise reduction is observed at ~ 0.01, 0.07, and 0.14 Hz, corresponding to tilt and compliance, the primary microseism, and the secondary microseism, respectively (Figure 3d). We test the order of corrections, comparing the final spectra when compliance is removed after tilt noise versus when tilt noise is removed after compliance noise. To first order, no difference is observed, and for the remaining analyses, *Z-corrected* spectra are calculated by first removing tilt and then compliance noise. The spectra for the seismic and pressure components grouped by experiment are shown on Figures S3-S7.

4.2 Average Coherences

For all BBOBS, we present the coherences between each horizontal and the vertical component, *H1-Z* and *H2-Z*, and the coherence between the pressure and vertical components, *P-Z* (Figure 4a-c). On the *H1-Z* and *H2-Z* pairs, we clearly observe high coherence values on a subset of the instruments at frequencies < 0.1 Hz with no clear dependence on water depth. This is consistent with tilt noise on the *Z* component. We observe high *P-Z* coherence with a water-depth-dependent high frequency limit that agrees with the predicted cutoff for infragravity waves. This is consistent with compliance noise on the *Z* component. We also observe a region of high *P-Z* coherence at frequencies at and just above ~ 0.14 Hz, consistent with the secondary microseism. Another, more moderate, peak observed at ~0.07 Hz is consistent with the primary microseism. We recalculate the *H1-Z* and *H2-Z* coherences after compliance noise removal, and the *P-Z* coherence after tilt noise removal from the *Z* component (Figure 4d-f). Since tilt is typically assumed to be the larger noise source, we expect its removal should result in a more visible compliance signal, and an increase in *P-Z* coherence. As anticipated, we observe that the *P-Z* coherence tends to increase after the removal of tilt noise at frequencies below the infragravity cutoff. However, we also observe an increase in the *H1-Z* and *H2-Z* coherences for some instruments when we first remove the compliance noise. This suggests that the two noise sources may have similar amplitudes at some stations, in contrast to the assumption that tilt noise is typically a much larger noise source (Bell et al., 2015). This is discussed further in Section 5.1.

Coherences between horizontal and pressure component pairs are typically not investigated for BBOBS noise characterization and removal, as incoherence is predicted (Crawford & Webb, 2000). We mostly observed *H1-P* and *H2-P* incoherence in our compiled dataset, with the exception of the shallowest stations, where coherences were > 0.5 near 0.1 Hz for both these component pairs (Figure S8). Tilt and compliance corrections for the *Z* component can still be used in this frequency band at these shallow water instruments (An et al., 2020; Webb & Crawford, 2010), as long as this coherence is accounted for.

4.3 Determinants of Station Noise

Our systematic calculation of the (dis)similarity between station noise spectra after subdividing stations by each metadata parameter yields quantitative estimates (in terms of "penalty", the measure of dissimilarity) of the relative importance of these features in controlling noise properties. A higher penalty reduction suggests that a given parameter is a better predictor of spectral characteristics. As a baseline, the mean penalty per trace for the *Z*, *Z-corrected*, and *H* components is 4.94, 4.27, and 4.46, respectively. We report "penalty reduction" as a percent deviation from these values.

4.3.1 1-Layer Analysis

We first discuss results for our 1-layer analysis (Figure 5a). The largest penalty reduction is obtained when grouping stations by "*Experiment*" (a mean penalty reduction of 17.4%, when averaging over the *Z*, *H*, and *Z-corrected* components). Next is "*Instrument Design*", which produced an average penalty reduction of 15.6%, and yields the largest penalty reduction for the *Z* component (19.8%). However, neither of these parameters directly illuminate the physical processes controlling seismic noise, as they strongly co-vary with other metadata. For example, 14 (out of 18) experiments involve only one type of instrument design and seismometer (Table S1). Experiments typically occupy a small footprint (Figure 1), so intra-experiment variation in the environment is also limited. Similarly, "*Instrument Design*" co-varies with "*Seismometer*", "*Water Depth*" (*e.g.*, TRM designs are only deployed in < 1000 m), and "*Pressure Gauge*". Nonetheless, the significant penalty reduction under these two parameters demonstrates that experiment and instrument parameters collectively have substantial impact on noise characteristics, reinforcing the need for careful deployment planning.

The *"Seismometer"* parameter has the next greatest influence on the noise spectra (Figure 5a), reducing the total penalty by ~10% for both *Z* and *H* components. For the *Z* component, the "*Seismometer"* subgroup spectra show different signatures of classic BBOBS noise (Figure 6). The CMG-3Ts display a power law (linear in log-log space) amplitude increase at frequencies below 0.1 Hz, characteristic of tilt noise. By contrast, T-240s and T-Compact subgroups have more spectral curvature and multiple inflection points at the same low frequencies, which is characteristic of compliance noise (Bell et al., 2015). The *H* spectra provide further insight (Figure 6c). All three seismometer subgroups show bottom current noise (an ~18dB/Hz-decade linear increase in log-log space at low frequencies). However, the subgroups of *H* spectra are clearly distinguished by their noise notch relative to their secondary microseism peak. The CMG-3Ts have the least distinct noise notch (just ~15 dB below the secondary microseism), and are the noisiest instruments, on average, at long periods, especially for horizontals. T-Compacts have an intermediate noise notch (~20dB below the secondary microseism), partially influenced by the substantial primary microseism associated with shallow water shielded instruments. T-240s have a noise notch ~30dB below the secondary microseism, and have the quietest horizontals at long periods. The average spectra for the *Z-corrected* components for the CMG-3Ts and the T-Compacts are nearly identical; however, long period noise on the T-240s remains ~ 20 dB quieter (Figure 6e).

In the higher-frequency band (0.1-1 Hz) dominated by the secondary microseism, the T-240s peak ~10 dB lower than the other sensors, on all components. This observation is somewhat surprising, as the secondary microseism peak is ubiquitous in all ocean environments and does not vary dramatically even with depth (Figure 6). We have considered the possibility that incorrect instrument gain(s) may contribute to this apparent offset (Doran & Laske, 2019), and tested the potential impact of this error on our results by adding a constant 10 dB to spectra that have an anomalously low secondary microseism peak. The overriding conclusion of our tests is that the quantitative subgroupings and associated interpretations are not sensitive to gain uncertainty of this magnitude, but this may slightly impact the absolute amplitude differences observed between different seismometers. We discuss these metadata uncertainties further below.

"Water Depth" has a similar level of influence on the noise spectra as the "*Seismometer"* parameter. These two categories are also parsimonious in their numbers of subgroups (2 and 3, respectively). *"Water Depth"* is particularly deterministic for *Z* component noise, with a penalty reduction of 14.1%, compared to 4.8% for *H*, and 4.0% for *Z-corrected* (Figure 5). Unlike for the "*Seismometer"* parameter, *"Water Depth"* subgroups were determined by grid search. The cutoff depths separating these subgroups are relatively shallow for all three components, between ~ 200 - 500 m depth. This cutoff separates shallow versus deep noise environments, reflecting the distinctive signal of shallow water infragravity waves in the 0.04 - 0.1 Hz band, likely due to direct wave loading that overlaps with primary microseism frequencies, observed on all components (Webb & Crawford, 2010; An et al., 2021). Our depth resolution is limited by the depths at which BBOBS were deployed; thus, we report the maximum and minimum depths of the shallow and deep subgroups, respectively (Figure 6). While this shallow water signal is present on all components, compliance noise continues to influence the *Z* component at lower frequencies (< 0.03 Hz), following the characteristic depth dependence of infragravity waves (Figure 4). This explains the greater penalty reduction for the *Z* component, relative to the *H* and *Z-corrected* components. A more detailed investigation of the grid search for the *Z* component indicates two depths where there are sharp changes in the penalty function: (1) the 200-500 m cutoff discussed above, and (2) an inflection at ~ 2600 m water depth (Figure S9). This may reflect the variable

frequencies of the compliance noise, and suggests broadly that categorization into shallow, mid-depths, and deep-water regimes is useful for predicting overall BBOBS noise levels for a deployment.

The remaining parameters are less useful singular determinants of noise characteristics, as they mostly have smaller penalty reductions (< 5% for each component). The penalty reductions for the *Z* component using *"Crustal Age*" and "*Distance from Land*" are somewhat higher; however, covariance with "*Water Depth"* likely explains this observation. Covariance amongst parameters is exemplified by the apparently perverse observation that "*Pressure Gauge*" has some apparent predictive power for the noise characteristics of the seismic components.

4.3.2 3-Layer Analysis

For the 1-layer analysis, the power of any single parameter to predict noise characteristics is limited, with 6.5% of variation explained, on average. This low value indicates the multifactorial controls on BBOBS noise. Therefore, we expand our analysis up to three layers to determine which combinations of parameters yield subgroupings with the most similar spectral characteristics. This also helps us test which parameters (if any) have a secondary role in regulating noise variability.

We start with a new baseline 2-layer analysis. We group stations by "*Seismometer*" (three subgroups), and then by *"Water Depth*" (two subgroups), yielding a total of six subgroups (Figure 7). These two parameters were chosen on the basis of their high penalty reduction (Section 4.3.1), their parsimonious subgroups, their relative lack of covariance with simpler parameters, and their clear physical relationships with noise, facilitating interpretation. The 2-layer analysis yielded a 20% average penalty reduction (horizontal lines in Figure 5b), with 27.4% for the *Z* component, 19.2% for the *H* components, and 13.5% for *Z-corrected*. As above, the larger penalty reduction for the *Z* component reflects its sensitivity to both compliance and tilt. This is further supported by the relatively low penalty reduction (*i.e.*, higher inter-group similarity) for the corrected vertical component (*Z-corrected*), which nominally has these effects removed. On the other hand, the fact that the *Z-corrected* component still has non-zero penalty reduction demonstrates that factors other than tilt and compliance influence noise characteristics, or that these corrections do not work perfectly. More sophisticated methods of noise removal, such as algorithms that account for temporal variability of the transfer functions, or iterative removal processes (Bell et al., 2015; Tian & Ritzwoller, 2017), might drive this "*Z-corrected*" penalty reduction down further.

We conducted independent grid searches for water depth cutoff values in each seismometer subgroup. The optimal depth cutoff for the T-Compact subgroup was between 354 - 430 m, very similar to the shallow cutoff depths discussed above (Figure 7). T-Compact seismometers are used in the majority of the shielded BBOBS instruments designed for shallow water deployments < 1000 m. By contrast, the T-240 and CMG-3T subgroups have deeper apparent cutoffs, between 2564 - 2687 m and 2785 - 2822 m, respectively. This is similar to the secondary mid-depth cutoff noted above. Since these subgroups do not include most of the shallow-water BBOBS, they do not include characteristically very shallow (< 500m depth) spectra, and so their intra-group grid searches find what we believe to be an important local minimum in penalty at ~2600m. Close investigation of the grid search results for the Trillium Compacts (Figure S9) reveals the same local inflection at ~2600 m cutoff depth.

Finally, we perform a 3-layer analysis. Each of the six subgroups from the 2-layer *"Seismometer"* and *"Water Depth"* analysis is further subdivided according to each of the remaining parameters (*e.g.*, Figure 7, Figures S10-12), and penalty reduction is measured. Aside from "*Experiment"* (see caveats below), "*Environment"* yields the highest 3-layer penalty reduction (25.8% mean reduction, or 5.8% above the 2-layer baseline, for all components). This is likely explained by differences in the frequency distribution of the secondary microseism across ocean basins (Babcock et al., 1994; Yang et al., 2012). "*Distance from Land*" is the numerical parameter that provided the highest penalty reduction, approximately 5.5% above the 2-layer baseline for all components. While not included in the main analysis, we test the effects of including "*Water Depth*" again in the third layer. It results in similar penalty reductions as "*Distance from Land",* which is likely a consequence of covariance between water depth and distance from land.

Other numerical parameters in the 3-layer analysis yield lower penalty reduction, but all improve upon the 2-layer baseline by > ~3%. The fact that several, rather than any one, of these parameters control noise characteristics is highlighted by the particularly high penalty reduction (9.9% above the 2-layer baseline across components) for *"Experiment"* in the 3-layer analysis. As discussed above, because individual experiments do not usually span large portions of metadata space, this parameter effectively combines many other parameters. Thus, it functions as a heuristic for the extent to which station noise is determined by all the station metadata collectively. One way of looking at this is as a lower bound for the aspects of station noise that are deterministically based on instrument type and location, with the remainder of variability owing to random site characteristics and spatiotemporally varying sea state. A final point of note is that moving from the 1- to 3-layer hierarchy, "*Instrument Design"* switches from providing the second highest to the second lowest penalty reduction. Of course, instrument design is strongly related to seismometer type and - via shielding - water depth. However, this result indicates that having controlled for covariance with those factors, the design of the instrument is not itself highly impactful on noise characteristics.

4.3.3 Significance of Observations

Finally, we consider the possibility that we observe penalty reduction simply by chance. We test the significance of the observed penalty reduction by computing the penalty reduction for 10,000 random subgroups of spectra. In each iteration, we keep the same number of subgroups and number of stations in each subgroup as in the true groupings analyzed above. However, instead of assigning stations into each subgroup according to their metadata parameters, we assign them randomly. Taking the example of the 3-layer analysis of "*Seismometer*", "*Water Depth*", and "*Distance from Land*", the random assignments yield a mean penalty per trace of 4.93 (the standard deviation is 0.02, and 95% of the random iterations yield a value above 4.89). This is only a 0.88% penalty reduction from the baseline (of 4.94), compared with the 32.7% penalty reduction when the data are grouped according to real parameters (which is 88 standard deviations removed from the baseline). This analysis establishes the strong significance of the relationships between metadata and station noise characteristics spectra (Figure S13).

4.4 Frequency and Amplitude Variability

While the previous analysis focuses on causes of inter-station variability in the noise spectra from 0.001 - 1 Hz, most seismic applications of BBOBS data use a band-limited frequency range. We calculate mean noise levels in four commonly used frequency bands. We focus on the following bands: (1) 0.1 - 1 Hz, centered over the secondary microseism band; (2) 0.05 - 0.1 Hz, centered over the primary microseism band and traditional noise notch in BBOBS instruments, both of which are relevant for ambient-noise analyses (*e.g.,* Zha et al., 2013; Russell et al., 2019; Yang et al., 2020), teleseismic body-wave imaging (*e.g.,* Wolfe et al., 2009; Hawley et al., 2016; Bodmer et al., 2018; Eilon & Abers, 2017), scattered-wave imaging (*e.g.,* Leahy et al., 2010; Janiszewski & Abers, 2015; Rychert et al., 2018; Mark et al, 2021), and shear-wave splitting (*e.g.,* Collins et al., 2012; Eilon et al., 2014; Bodmer et al., 2015; Lynner & Bodmer, 2017); (3) 0.01 - 0.05 Hz, the primary band for teleseismic long-period body- and surface-wave velocity and attenuation imaging (*e.g.,* Weeraratne et al., 2007; Laske et al., 2011; Jin et al., 2015; Cai et al., 2018; Janiszewski et al., 2019); (4) 0.005 - 0.01 Hz, of interest for very long-period surface wave (*e.g.,* Lin et al., 2016) and normal-mode (*e.g.,* Bécel et al., 2011) studies.

Based on the spectral angle analysis in the previous section, we plot noise levels as a function of water depth, parsed according to seismometer and instrument design (Figure 8). This analysis complements our spectral angle approach by comparing average absolute amplitudes in discrete frequency bands, rather than amplitude-agnostic spectral shape. Figure 8 illuminates several points that should be considered carefully during experiment design. First, there are no clear trends in noise level as a function of water depth, seismometer, or instrument type in the secondary microseism band (0.1 - 1 Hz). Most BBOBS tend to cluster near the NHNM (Peterson, 1993) in this range for both the vertical and horizontal components. Importantly, this is true even for the shallowest BBOBS, as this band is largely above the frequencies at which compliance noise is present. Some instruments display noise levels up to ~ 50 dB quieter on average, but it is possible that instrument-gain uncertainty contributes to these outliers (Doran & Laske, 2019).

In the primary microseism band (0.05-0.1 Hz), *Z* and *H* component noise levels increase for shallow BBOBS, consistent with direct seafloor loading due to infragravity waves; this effect is reduced for the *Z-corrected* component, but relatively high noise levels at the shallowest depths persist even after corrections. For each component, shallow water instruments have the highest noise levels in this frequency range.

In the lower frequency bands (< 0.05 Hz), the effect of compliance noise, in addition to tilt, is observed on the *Z* components, evidenced by the dependence on water depth. In contrast, the *H* components as a whole do not show a clear dependence on water depth in these bands; this may reflect the effectiveness of instrument shielding in mitigating strong shallow seafloor currents, and/or the fact that seafloor currents are pervasive at all ocean depths. The CMG-3T seismometers show a stronger trend of decreasing noise levels with water depth relative to the other seismometers, indicating that this trend may depend on instrumentation; however, further analysis is needed to assess the significance of this observation. The compliance and tilt corrections are generally effective in these bands, and the *Z-corrected* noise levels are largely distributed between the NLNM and the NHNM.

On average, BBOBS containing T-240 seismometers have the quietest noise levels at all frequency bands, but the differences become more pronounced at lower frequencies. This observation holds even accounting for the possibility of gain errors in some T-240 deployments (Doran & Laske, 2019). Importantly, this difference remains after tilt and compliance removal; that is, T-240s have, on average, the quietest *Z-corrected* components, with many deployments showing noise characteristics just above the NLNM. At frequencies lower than 0.1 Hz, BBOBS that contain a CMG-3T seismometer show higher noise levels than BBOBS with other sensors, particularly on the *H* components. The exaggeration of this effect at frequencies lower than 0.1 Hz is consistent with the presence of bottom current and tilt noise.

5. Discussion

Station metadata are strongly predictive of BBOBS noise characteristics. When stations are grouped by metadata parameters, there is substantially more similarity between spectra within those groups compared to the similarity averaged across the whole dataset (Figures 5 and 7). The water depth and seismometer type are the two most important factors that determine noise characteristics. The covariance between seismometer and instrument design complicates understanding the relative roles of these two parameters. However, consideration of these results may be useful during experiment design. For instance, if analysis relies upon 0.05 - 0.1 Hz period teleseismic *S-p* converted phases to evaluate mantle discontinuities, it is ill-advised to deploy in < 500 m water depths, as these signals will likely be dominated by noise that persists after tilt and compliance corrections. Similarly, CMG-3Ts seem to be the most noise-prone seismometers across a range of environments. Here we further discuss sources of noise, implications for data quality and traditional noise corrections, limitations of our analysis, and potential next steps for the BBOBS community.

5.1 Tilt and Compliance Noise

We have already suggested that the strong link between noise characteristics, and the seismometer and water depth parameters is primarily driven by variations in the tilt and compliance effects, respectively. Here we investigate how coherence between components can illuminate the relative roles of these noise sources as a function of seismometer, water depth, and instrument design. Importantly, the coherence is insensitive to any gain errors. We also discuss how these may affect noise removal approaches.

Compliance noise is characterized by high average *P-Z* coherence from ~0.005 Hz (due to our instrument response removal procedure) up to the theoretical infragravity frequency limit

(Crawford & Webb, 2000). Figure 4 shows very good agreement between the high-frequency limit of *P-Z* coherence and the predicted cutoff frequency at water depths spanning the full range from 0-6000 m. Unsurprisingly, water depth is a primary factor in determining a station's compliance noise signature. We estimate the presence of tilt noise from the maximum average coherence (in the range 0.005 - 0.035 Hz) between the *H1-Z* and *H2-Z* components. We follow the method of Bell et al. (2015), grid searching through horizontal component azimuths to find the orientation (theoretically the physical tilt direction) that gives the maximum coherence with the vertical (H_{tilt}).

First, we observe that Z-H_{tilt} coherence is higher on instruments with CMG-3T seismometers (Figure 9), consistent with their higher propensity for tilt noise. On average, the coherence is ~ 0.8, above the typical benchmark value used for tilt removal (Bell et al., 2015; Tian & Ritzwoller, 2017). This higher tilt noise could arise from higher susceptibility of these instruments to current noise, and/or a tendency of these instruments to remain slightly out of level (*i.e.*, to have a *Z* component that is not perfectly vertical). The analyses in Section 4.3 suggest that a combination of these effects may be important. While all seismometer types show similar low-frequency noise with a log-linear slope below 0.03 Hz on the *H* components, indicative of bottom current noise, amplitudes are systematically higher on CMG-3T seismometers (Figure 6), suggesting that these sensors are more strongly impacted directly by currents. In addition, only this seismometer shows this log-linear trend on the *Z* component (Figure 6), suggesting that it more commonly transfers current noise into *Z*-component tilt noise. Bell et al. (2015) also reported high tilt noise on these seismometers using data from just the first year of the Cascadia Initiative deployment, and suggested a tendency for their tilt direction to preferentially align with *H1*. Using our expanded dataset, we observe no systematic tilt direction (Figure 9). In contrast to this high tilt susceptibility, BBOBSs that use either the T-Compacts or T-240s have mean Z-H_{tilt} coherences that are < 0.5, lower than typical benchmark values for useful tilt noise removal (Bell et al., 2015; Tian & Ritzwoller, 2017). The T-Compacts offer the next highest $Z\text{-}H_{tilt}$ coherence after the CMG-3T seismometers; of these, average coherence for the TRM and AB shielded designs is particularly low, supporting the suggestion that shielding protects against horizontal noise contamination. However, unshielded BBOBSs using the T-240s also have comparably low values, suggesting that these seismometers may simply be less susceptible to tilt noise.

Tilt noise is typically assumed to be higher amplitude than compliance noise, but is not always present. Compliance noise is always present but may be masked by strong tilt noise (Crawford & Webb, 2000). It is therefore conventional to first remove tilt noise, which should lead to an increase in the *P-Z* coherence allowing for subsequent removal of the compliance noise. Our analysis (Figure 9) suggests this sequence of noise removal is particularly important for stations with CMG-3Ts. On the other hand, Tian & Ritzwoller (2017) find that both tilt and compliance noise interfere with each other (that is *H1-Z* and *H2-Z* coherence increases after compliance removal, and *P-Z* coherence increases after tilt removal), consistent with relative similarity in their strength. They suggest that multiple iterations of corrections may be appropriate in such cases. To investigate this systematically, we compare the *P-Z* coherence before and after tilt correction (Figure 10a), and *H1-Z* and *H2-Z* coherences before and after compliance correction (Figure 10b, c). For consistency between the two, we report the average coherence over the frequency range where compliance effects are present, which is inclusive of the range where tilt noise is expected for all stations.

As expected, the *P-Z* coherence increases for most instruments after tilt noise removal (Figure 10a), validating conventional noise removal approaches (*e.g.*, Wei et al., 2015; Accardo et al., 2017; Cai et al., 2018; Janiszewski et al., 2019). This test also reinforces the predominance of tilt effects on CMG-3T instruments: these seismometers have the largest gains in *P-Z* coherence, but see essentially no change in compliance-corrected *H1-Z* or *H2-Z* coherences (Figure 10b). In contrast, for instruments with Trillium seismometers, we find increases in both the tilt-corrected *P-Z* coherence and compliance-corrected *H1-Z* and *H2-Z* coherences. This suggests that at individual instruments either the two noise sources are similar in amplitude and interfere with one another, or that in some cases compliance removal may improve the ability to distinguish tilt noise on an instrument. A more detailed analysis of individual instruments is necessary to distinguish between these end member behaviors. In addition, recalculation of the tilt orientation after compliance removal, and testing of iterative noise removal methods may further help to determine properties and best practices related to the noise and its removal, but is beyond the scope of this study (Tian & Ritzwoller, 2017). Furthermore, whether this behavior remains stationary throughout the deployment of an instrument remains unclear.

Lastly, coherence actually decreases after noise removal at a subset of the TRM and AB instruments (Figure 10). These instruments have mostly high (> 0.5) *P-Z* coherences in the expected frequency range for compliance noise. We reiterate that these instruments also have high *H1-Z* and *H2-Z* coherences in the primary microseism band (Figure 4); the lower (< 0.5.) values observed here stem from averaging over the entire compliance frequency band, which is wider than the microseism. For such a decrease in coherence to occur, the noise across all four components of the BBOBSs must be coherent, which is a property only observed on shallow water instruments. With the exception of one AR instrument that may be affected by an error, all instruments that have a decrease in coherence are deployed in less than 280 m water depth.

5.2 Shallow Water Instruments

Shallow water BBOBSs have demonstrably distinct noise characteristics (Figure 6; Webb & Crawford, 2010; An et al., 2021). Since this is one of the strongest defining characteristics of observed BBOBS noise, here we further investigate if these characteristics are present on all shallow water instruments. Given the set of water depths chosen as the optimal division between shallow and deep instrument noise characteristics (e.g., Section 4.3), we suggest < 500 m depth as a conservative limit below which shallow water noise characteristics should be expected. These spectra typically contain a high amplitude peak on all components within the primary microseism band, extending to the predicted infragravity wave cutoff frequency. This peak is reduced, but not removed, by noise corrections (Figure 6). Within this band, pressure coherence with all seismic components of the BBOBSs is high (Figure 4; Figure S8) due to both vertical and horizontal loading of the seafloor from ocean waves directly above the instrument (Webb & Crawford, 2010).

Only three experiments in our dataset deployed instruments at depths < 500 m: the Alaska-Aleutians Community Seismic Experiment (AACSE), located offshore Alaska; the Cascadia Initiative (CI), located offshore the northwest coast of the United States; and SEGMeNT, located in Lake Malawi in Africa. The former two share environmental similarities: the continental shelf adjacent to the Pacific Ocean basin. Their noise characteristics are also similar (Figure FS14); the majority of these shallow BBOBSs contain the expected high amplitude peak on vertical and horizontal components at ~ 0.07 Hz. In contrast, this feature is much weaker at the Lake Malawi stations (Figure FS14), which record the primary ocean microseism in the far field. Lake Malawi stations instead manifest a strong noise peak at 0.3-1.6 Hz (Carchedi et al., 2022). This is likely due to differences in the characteristic wavelength of wind-driven waves in lacustrine versus oceanic settings. While microseisms are generated at lakes, they have distinctively higher frequencies than those generated in the oceans (Xu et al., 2017; Smalls et al., 2019) explaining the strong 0.3-1.6 Hz peak (Carchedi at al., 2022). Lake infragravity waves are also present (Accardo et al, 2017), seen from 0.02-0.06 Hz (Figure S14).

Importantly, these differences may impact the application of different seismic analysis techniques on the data. For example, at Lake Malawi the separation of the ocean microseism from both the lake-generated microseism at higher frequency and lake infragravity waves at lower frequency allowed Accardo et al. (2017) to observe clear ambient noise cross-correlation signals between lake-bottom and land seismometers in the 0.04-0.125 Hz range, including at those instruments deployed at depths < 500 m. By contrast, ambient noise cross-correlations from shallow-water instruments in Cascadia had low signal-to-noise ratios at these frequencies (Janiszewski et al., 2019; Tian & Ritzwoller, 2017), due to local ocean-generated waves swamping the microseism signal.

5.3 Limitations

Although this study constitutes the largest systematic review of BBOBS noise characteristics conducted to date, there are important limitations to the dataset. Chief among these is that US BBOBS deployments using modern instrumentation have unevenly sampled large swaths of the metadata parameter space. For instance, there is more data from the Pacific Ocean than elsewhere, and a relative paucity of stations atop thick sediments or at great distance from coastlines (Figures S1, S2). A corollary to this uneven sampling is covariance in several station parameters, which makes it more challenging to tease apart the individual influences of, say, shielding versus shallow water on noise. Although we have attempted to pick apart the most important parameters controlling noise characteristics (Section 4.3), intrinsic covariation makes it impossible to separate parameters completely. This is most clearly seen from Figure 5 where the "*Experiment*" is the most important parameter determining noise characteristics, simply because the small geographic footprint of most experiments means that other station parameters are alike within each experiment, and most experiments use a homogeneous instrument design. A small number of co-located pilot deployments of BBOBS with different seismometers or instrument designs in shallow and deep locations could test the robustness of the results presented here. We also suggest that co-deployments should be an essential aspect of testing new BBOBS designs whenever possible.

Our analysis is dependent on the accuracy of both data and metadata archived within the IRIS DMC, and one example of a co-located deployment suggests that errors may exist. The PLUME experiment (Doran & Laske, 2019) utilized an intermixed array of T-240 and CMG-3T sensors in relatively deep water. The individual seismometer spectra (Figures S3-S4) group into distinct clusters, with the T-240s offset to significantly lower power at all bands. Given the similar deployment environment for these instruments, the simplest interpretation for the offset is a gain error. Based on the secondary microseism peak (0.1-1 Hz), the CMG-3Ts are biased ~10 dB too high, or the T-240s are biased low. Doran & Laske (2019) analyzed this apparent bias and calculated station-specific gain corrections of x2 or x4 for the PLUME T-240 observations.

Here, we take a more general approach to specifically assess whether such issues could significantly impact our analyses. We estimate that the T-240 data are biased approximately 10 dB low. This is based on the observations that the average T-240 spectrum is lower than our full-dataset average in the secondary microseism band by approximately this amount (Figure 6), and that several older T-240 experiments have low noise levels relative to more recent experiments using those same instruments, including in the secondary microseism band (Figures S3-S4).

To test the impact of these gain uncertainties on our analysis, we collect all the T-240 spectra from these suspect experiments collected prior to 2011, and increase them by 10 dB. We then re-run the spectral-angle analysis, and compare the resulting groupings to those presented above (Section 4.3). The dominant groupings are unchanged, as are the majority of the details of the spectral characteristics within each grouping. The weaker secondary microseism peak in the average T-240 spectrum is no longer present, but the T-240 spectrum at long periods remains lower than the other instruments, particularly for the *Z* and *Z-corrected* components. After this adjustment, the difference between the *H* component noise on the T-240 and T-Compact is minimal; however, both remain lower than the observed noise levels for the CMG-3Ts. This evaluation reassures us that our primary conclusions are robust in the face of metadata uncertainty of the scale suggested by Figures S3-S4.

Finally, the limited duration of standard OBS deployments (≤ 12 months) means that our analysis is subject to the idiosyncrasies of experiment timing. As an example, the recording period for the HOBITSS experiment on the Hikurangi forearc largely overlapped the 2014-2016 El Niño event, confounding our ability to assess the normative noise characteristics of this particular margin. In this study of overall trends, we have chosen not to consider seasonal variability of noise, which can be substantial (*e.g.*, Grob *et al*., 2011), and in addition we do not consider secular changes in noise with time (*cf.* Bell *et al.*, 2015). Further, this study uses only instruments from US-funded BBOBS deployments; many other designs exist that we have not included here. Their future inclusion would likely mitigate covariances between metadata parameters (particularly between seismometer and instrument design), and yield a wider geographic footprint.

As the marine geophysical community plans for long-term BBOBS observatories (Kohler et al., 2020), it would be worthwhile to invest resources in exploring the noise characteristics of these under-sampled regions of metadata parameter space. The dataset presented in this study assists in framing noise domain gaps that future pilot experiments could fill.

6. Conclusions

We have computed representative noise spectra for 551 broadband BBOBS stations spanning 18 experiments deployed between 2005 – 2019, including seismic components and pressure gauges. We also calculated cross-spectral properties (admittance, phase, coherence) that help reveal and quantify seismic noise induced by bottom currents and infragravity waves. The resultant dataset constitutes the most comprehensive sampling of noise characteristics at seafloor stations to date. Our analysis supplies a framework for BBOBS users to compare and assess the noise characteristics of individual datasets, better anticipate noise characteristics for newly acquired data, and provide a baseline catalog that will continue to grow in detail and utility as the marine geophysics community expands BBOBS sampling of the world's diverse seafloor.

By grouping noise spectra based on metadata parameters, we demonstrate that there are significant systematics to BBOBS noise characteristics. The most important determinants of noise characteristics are the seismometer (which strongly covaries with instrument design), and the water depth at which it is deployed. Accounting for other factors, BBOBSs with CMG-3T seismometers seem to have higher low-frequency noise than average, and those with T-240 sensors have lower noise levels, particularly on the vertical components. CMG-3T instruments have higher tilt noise on the vertical components, most clearly seen at long periods, and overall, more noisy horizontals. Although noise is correlated with seismometer (and by extension instrument design) type, we find no systematic orientation of the tilt noise, suggesting that none of the BBOBSs' engineering creates a bias in tilt direction.

We have shown, for the first time, that the theoretical depth-frequency limit for seafloor compliance is closely matched by the data spanning 0-6000 m in water depth. BBOBS deployed on continental shelves in shallow water (< 500 m) have systematically different noise properties, characterized in particular by higher noise in the primary microseism band on all four components. The exception is shallow water lake instruments, which have low noise in the global microseism band, and a unique ~ 0.4Hz peak. This and other departures from our main groupings will need to be reevaluated in the future as new datasets provide wider sampling of station properties.

We found that grouping by experiment yielded the highest similarity of spectra, indicating that the combination of station parameters (similar instrumentation, geographic footprint, etc.) deterministically controls overall BBOBS noise. This holds promise for informed experiment planning; overall noise properties are station contingent, but largely predictable. Despite this, we recognize that our analysis is incomplete, limited by uneven global sampling, and covariance between important metadata parameters. Key future work may include systematic analysis of seasonal and other temporal variability, expansion of the dataset to include additional instrument designs and deployment locations, including non-US-funded deployments, buried or cabled instrumentation, and testing the effects of iterative noise removal procedures.

Acknowledgements: Data used in this research were provided by instruments from the Ocean Bottom Seismic Instrument Center (https://obsic.whoi.edu), which is funded by the National Science Foundation (https://www.nsf.gov), and the Ocean Bottom Seismograph Instrument Pool (OBSIP). We thank the instrument center staff at Woods Hole Oceanographic Institution (WHOI), Lamont Doherty Earth Observatory (LDEO), and Scripps Oceanographic Institution (SIO), as well as seagoing technicians and scientists who made collection of this data possible. These data are archived at the IRIS Data Management Center (http://www.iris.edu). This manuscript benefited from conversations with Spahr Webb, and Kasey Aderhold. This work was funded by National Science Foundation Awards OCE-1658491, OCE-1658214, and OCE-1753722.

Author Contribution Statement: HAJ designed and coordinated the study, carried out the processing and calculation of spectral properties for all instruments, organized all data for analysis. ZE assisted in study design and coordination of the writing. JR aided in processing of YOUNG ORCA data. BB, ZE, HAJ, and SC designed and carried out the spectral angle analysis. HAJ, JR, ZE, JG, SM, WH each contributed to the collection of metadata parameters for the stations. All authors participated in interpretation and manuscript preparation.

Data Availability Statement: The seismic and pressure time series data are available for download through the IRIS Data Management Center (http://www.iris.edu). The assembled station metadata table, and calculated spectral properties are available in the online supplementary material. Additionally, the calculated noise spectra and cross spectra, and metadata table will archived at Dryad, currently available upon request. The ATaCR package used to process the data is available here: https://github.com/helenjanisz/ATaCR.

Figures and Tables

Table 1: Information related to different BBOBS instrument types included in this study, including defined abbreviations to distinguish them.

Abbreviation	Design Institution	Seismometer	Pressure Gauge	Shielding	Instrument Name
AB	SIO	T-Compact	DPG	Syntactic Foam	Abalone
B2	SIO	T-240	DPG	None	SIO Unshielded Broadband
BA	LDEO	T-Compact	APG	None	LDEO Unshielded APG Broadband
BD	LDEO	T-Compact	DPG	None	LDEO Unshielded DPG Broadband
TRM	LDEO	T-Compact	APG	Steel Plates	LDEO Trawl Resistant Mount OBS
AR	WHOI	T-Compact	DPG	None	WHOI ARRA
BG	WHOI	CMG-3T	DPG	None	WHOI BBOBS
KE	WHOI	CMG-3T	DPG	None	WHOI KECK[1]

Note: 1. The WHOI KECK also includes a strong-motion accelerometer distinguishing it from the WHOI BBOBS.

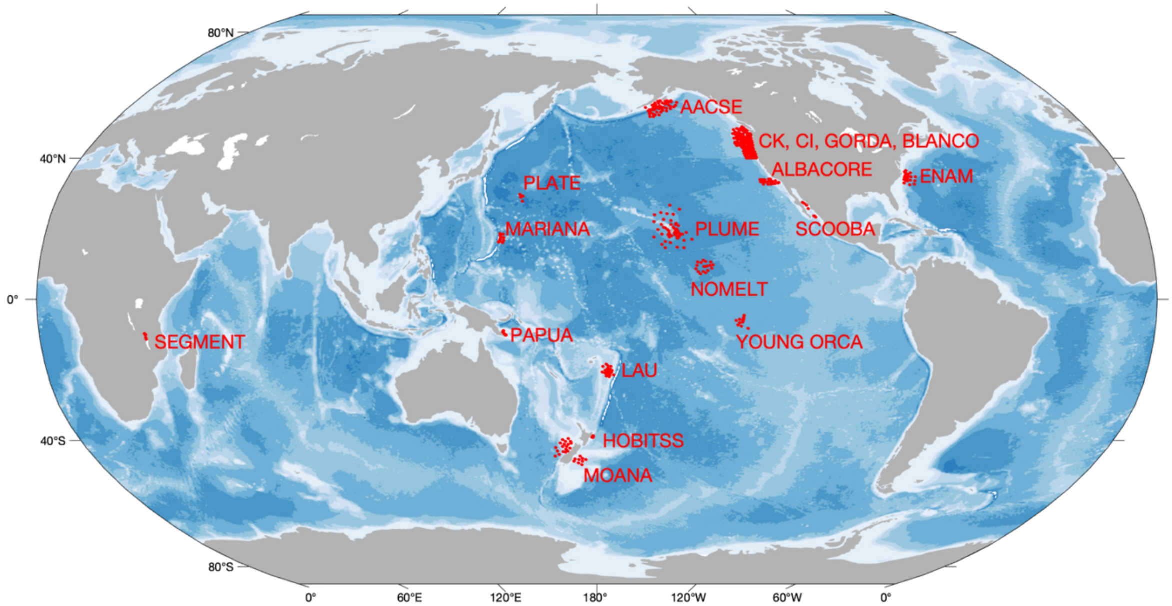

Figure 1: Map of analyzed BBOBSs (red circles). Details corresponding to each deployment are given in Table S1. Made using M_Map (Pawlowicz, 2020).

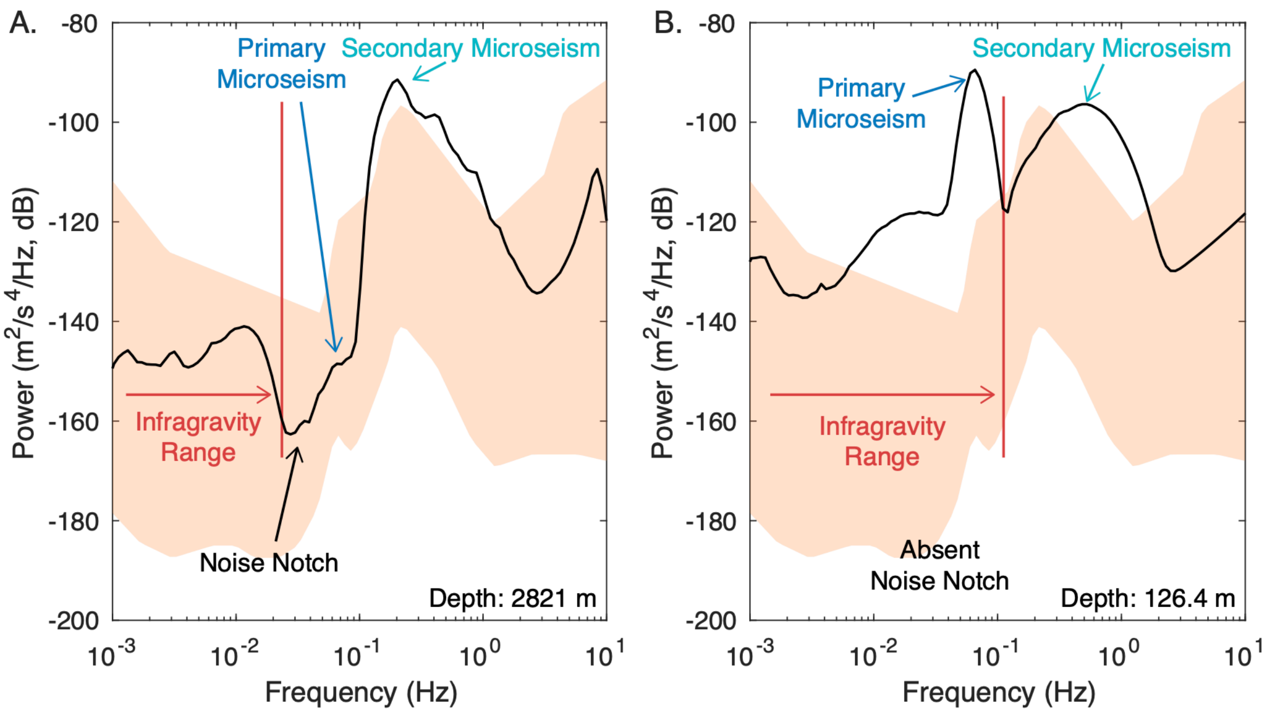

Figure 2: Examples of noise spectra for the *Z* component of a BBOBS for (a) deep-water station J36A and (b) shallow-water station M08A, both from the Cascadia Initiative. The primary, and secondary microseism peaks, the noise notch, and the infragravity band are labeled. The Peterson (1993) high and low noise ranges are shown as the orange shaded area.

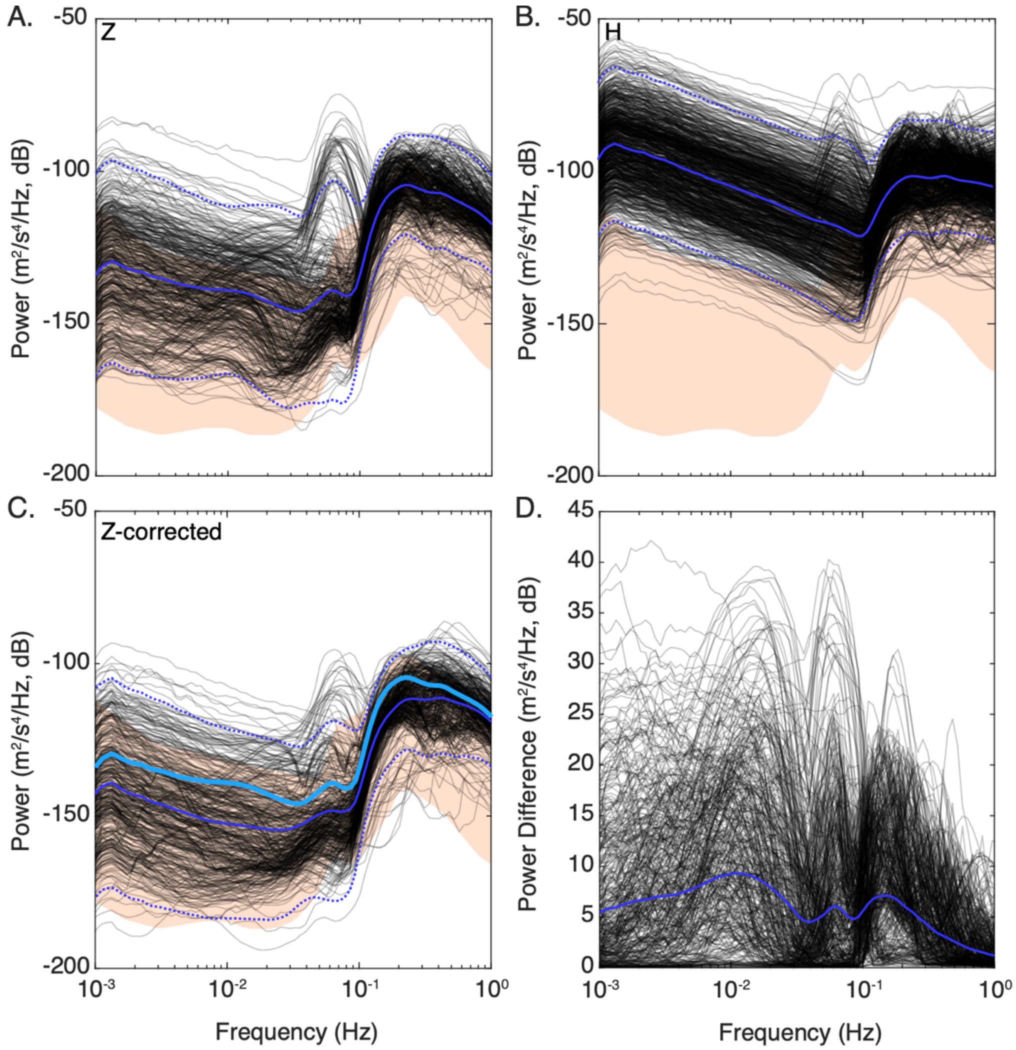

Figure 3: Power spectra for (a) *Z*, (b) *H*, and (c) *Z-corrected* for all individual stations. Solid and dashed dark blue lines indicate mean and 2-σ standard deviations, respectively. Solid light blue line on (c) is the uncorrected *Z* mean for comparison. The Peterson (1993) high and low noise ranges are shown as the orange shaded area. (d) Difference between the *Z* and *Z-corrected* spectra; positive values indicate lower values for the corrected dataset. The dark blue line indicates the mean difference.

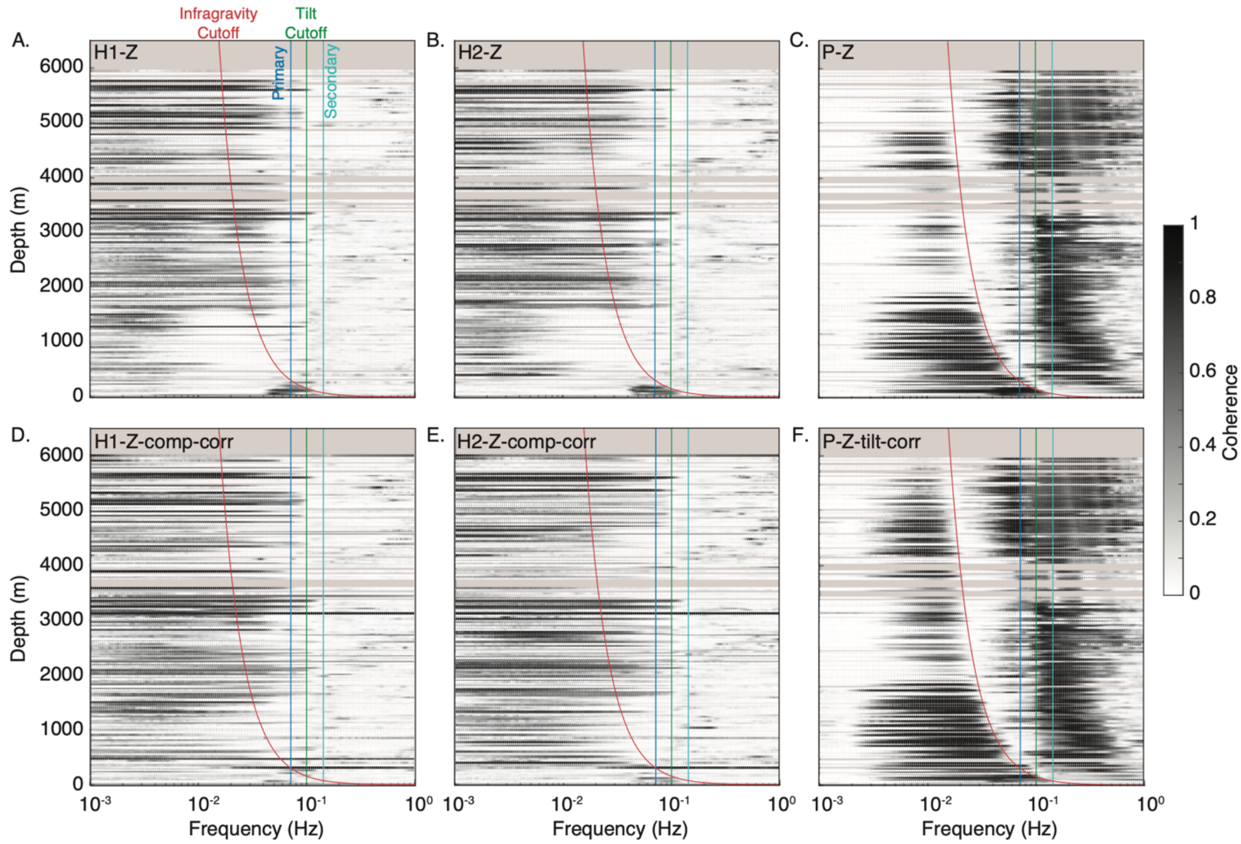

Figure 4: Coherences of the *H1*, *H2*, and *P* with the *Z* for each BBOBS compared with the water depth of the instrument. The red line indicates the predicted infragravity cutoff frequency (*f*) as a function of water depth (*d*), using the equation $f = \sqrt{\frac{g}{2\pi d}}$ (Bell et al., 2015); the green, dark blue, and light blue lines indicate the tilt cutoff (0.1 Hz), primary (0.07 Hz), and secondary (0.14 Hz) microseism peaks respectively. (a-c) Coherences calculated with the *Z* component; (d-e) *H1-Z* and *H2-Z* coherences with the *Z-compliance-corrected* component; (f) *P-Z* coherence with the *Z-tilt-corrected* component.

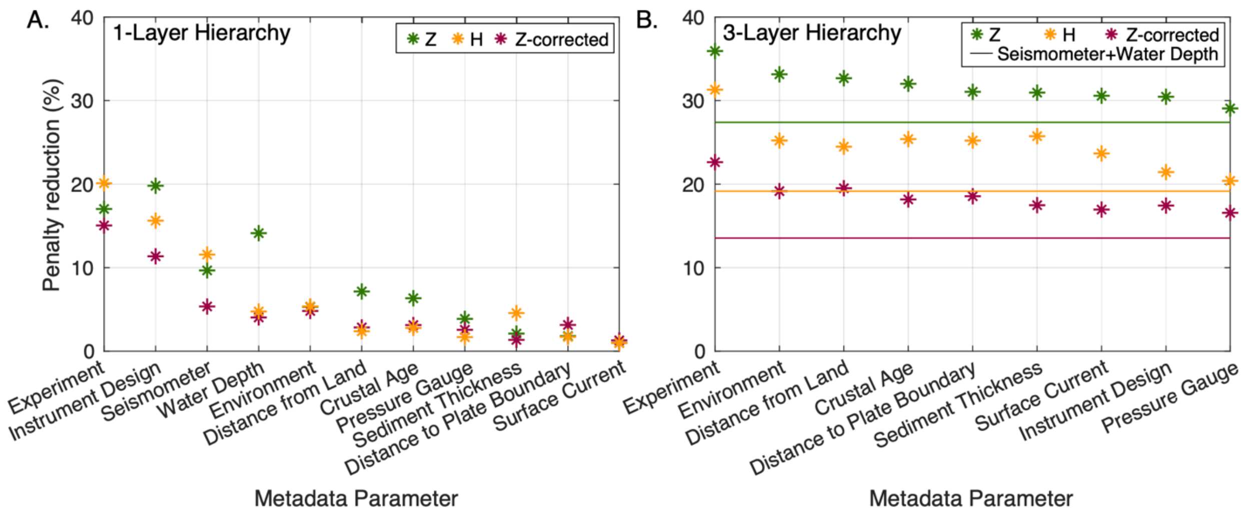

Figure 5: Percentage penalty reduction in spectral angle for *Z*, *H*, and *Z-corrected* for each metadata parameter subdivision. Larger reductions indicate more similarity within the final subgroups. Parameters are sorted from left to right in descending order of their average penalty reductions. (a) Results for each metadata parameter (1-layer analysis). (b) Results after subgrouping the BBOBS by "*Seismometer*", then "*Water Depth"*, and then the labeled metadata parameter (3-layer analysis). The 2-layer penalty reductions for "*Seismometer*" and "*Water Depth"* are shown by the solid lines.

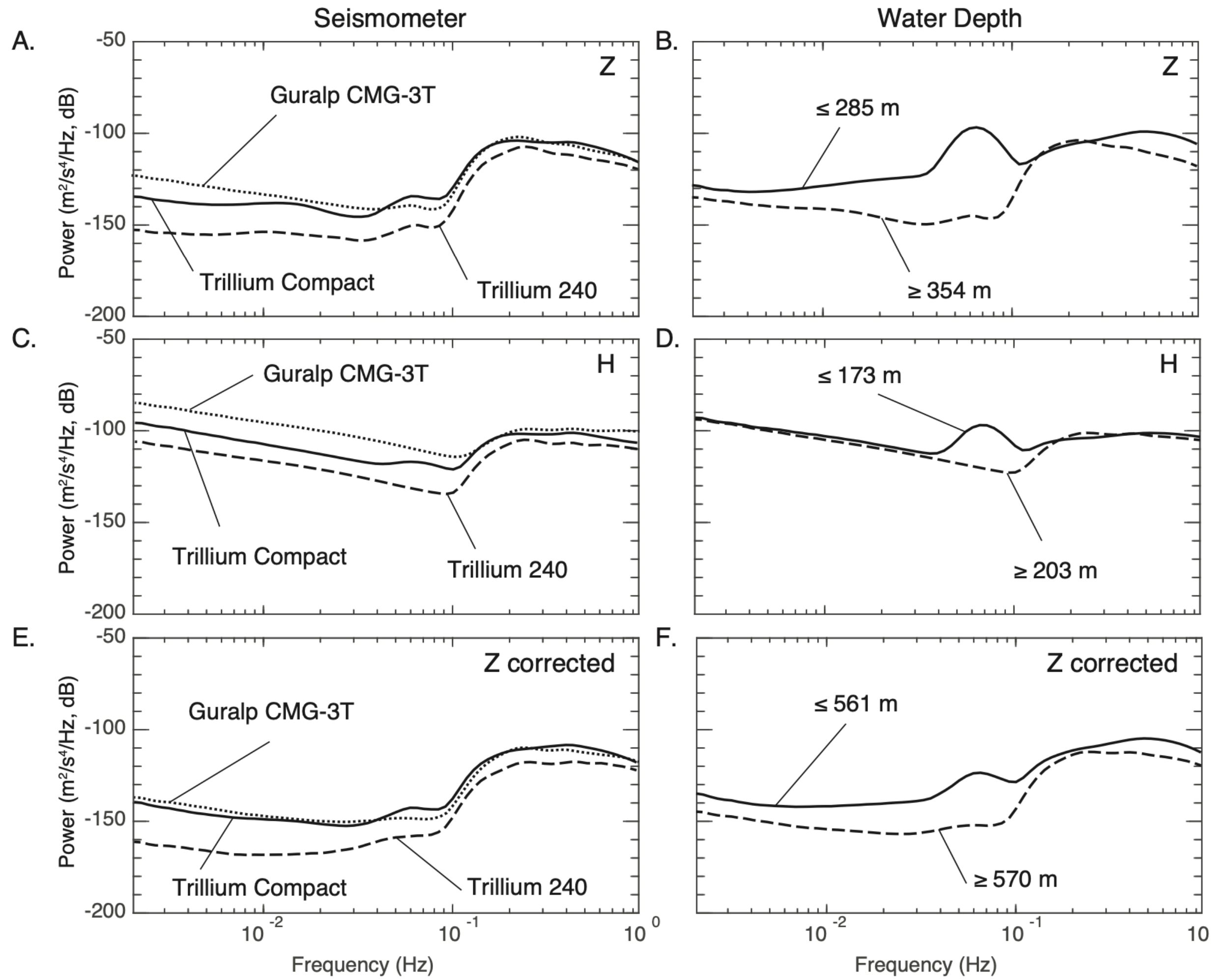

Figure 6: Average spectra calculated from the resultant metadata subgroups based on "*Seismometer*" and *"Water Depth"*. (a) The average *Z* spectra for the three "*Seismometer"* subgroups: CMG-3T, T-Compact, and T-240. (b) The average *Z* spectra for the two *"Water Depth"* subgroups (grid search determined cutoff depths indicated). (c) Same as (a), but for the *H* components. (d) Same as (b), but for the *H* components. (e) Same as (a), but for the *Z-corrected* component. (f) Same as (b), but for the *Z-corrected* component.

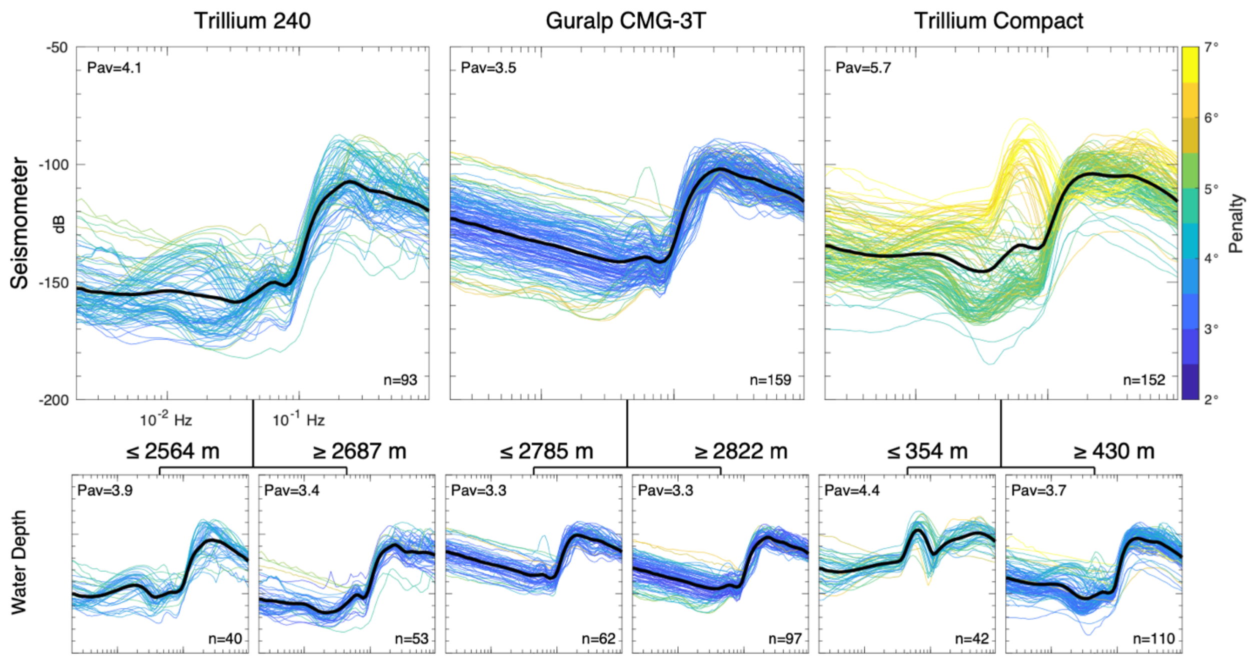

Figure 7: Example of subgrouping by spectral similarity, showing the 2-layer analysis for *Z* spectra. These were first subgrouped by "*Seismometer"*, then subgrouped by *"Water Depth"*. The seismometer types and threshold depths are indicated above each plotted subgroup. For each subgroup, the average spectrum is plotted in black. Individual spectra are colored according to their average spectral angle (*i.e.,* penalty) from the other spectra in that subgroup. The same vertical and horizontal scale is used for all plots. The number of spectra (n) and the average penalty (Pav) for each subgroup is given in the corresponding plots.

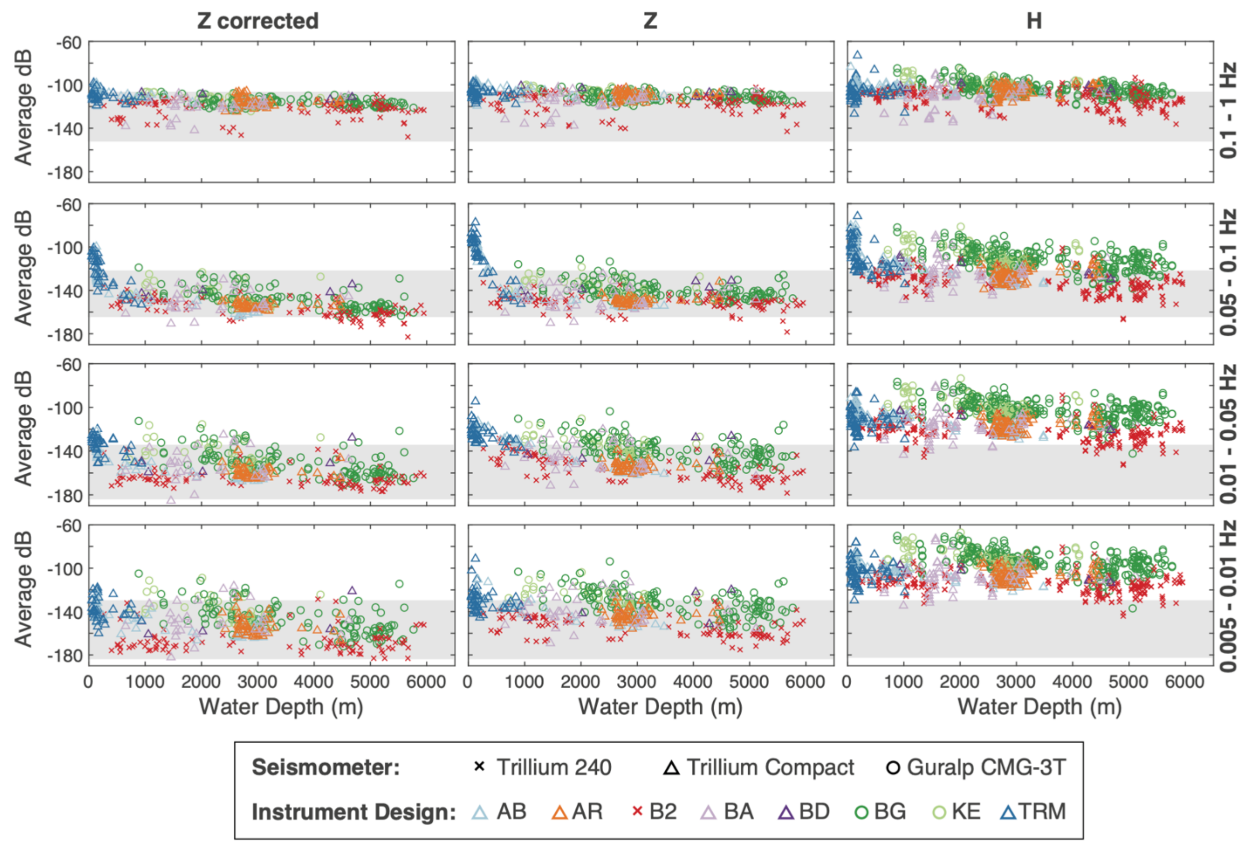

Figure 8: Average power for the *Z*, *H*, and *Z-corrected* components plotted as a function of water depth for each BBOBS in four frequency bands (ranges shown on right). Symbols indicate the seismometer; colors indicate the instrument design (see Table 1 for more details). Gray shading indicates the average Peterson (1993) high and low noise model range in each frequency band.

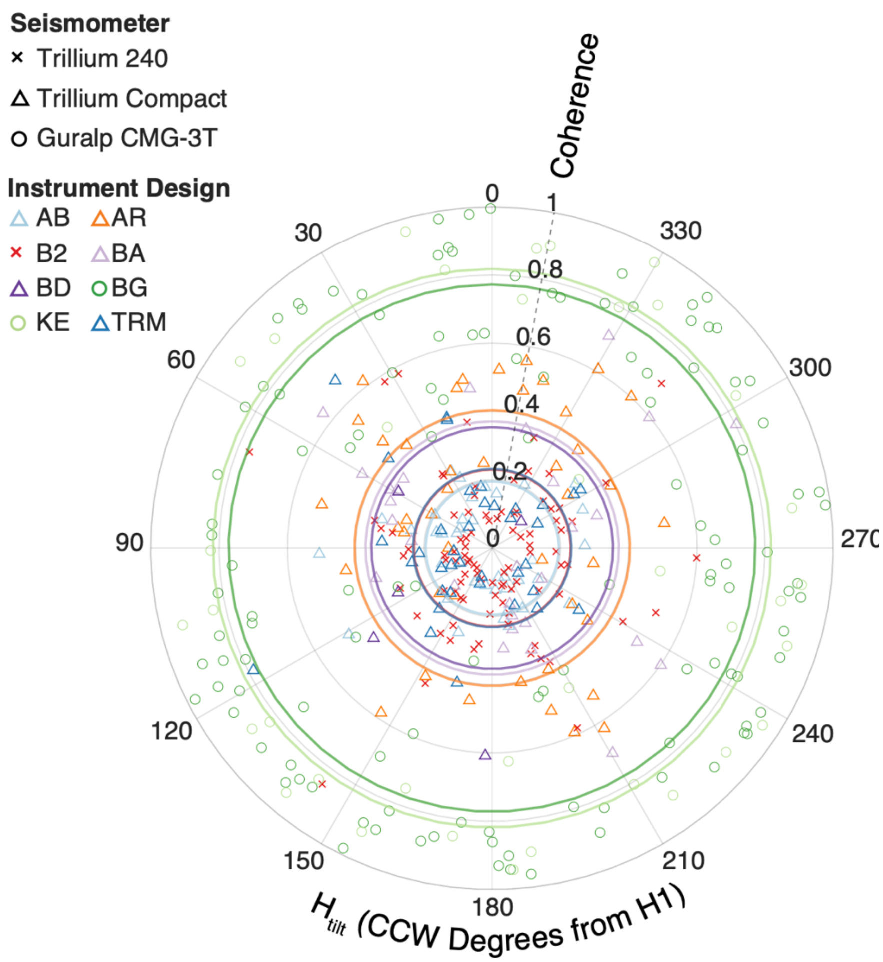

Figure 9: The tilt orientation (H_{tilt}), measured as a function of degrees counterclockwise from *H1*, and the corresponding H_{tilt}-Z coherence for each BBOBS. Symbols and colors indicate seismometer and instrument design. Colored lines show the average H_{tilt}-Z coherence for each instrument design.

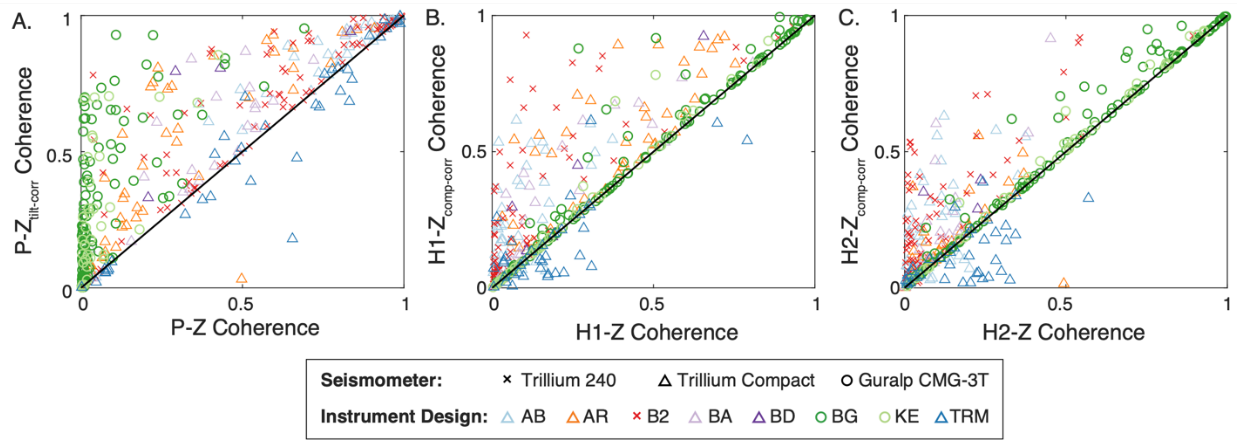

Figure 10: Comparison of coherences before and after tilt or compliance corrections. Symbols and colors indicate seismometer and instrument type; symbols that plot above the black line indicate an increase in coherence after corrections, below the line indicate a decrease in coherence, and along the line indicate no change. (a) Comparison of the *P-Z* and *P-Z-tilt-corrected* coherences. (b) Comparison of the *H1-Z* and *H1-Z-compliance-corrected* coherences. (c) Comparison of the *H2-Z* and *H2-Z-compliance-corrected* coherences.

Works Cited

Accardo, N. J., Gaherty, J. B., Shillington, D. J., Ebinger, C. J., Nyblade, A. A., Mbogoni, G. J., et al. (2017). Surface wave imaging of the weakly extended Malawi Rift from ambient-noise and teleseismic Rayleigh waves from onshore and lake-bottom seismometers. Geophysical Journal International, 209(3), 1892–1905. https://doi.org/10.1093/gji/ggx133

Aderhold, K, Woodward, R., & Frassetto, A. (2019). Ocean Bottom Seismograph Instrument Pool Final Report. Zenodo. https://doi.org/10.5281/zenodo.3524424

An, C., Wei, S. S., Cai, C., & Yue, H. (2020). Frequency Limit for the Pressure Compliance Correction of Ocean-Bottom Seismic Data. Seismological Research Letters. https://doi.org/10.1785/0220190259

An, C., Cai, C., Zhou, L., & Yang, T. (2021). Characteristics of Low-Frequency Horizontal Noise of Ocean-Bottom Seismic Data. Seismological Research Letters. https://doi.org/10.1785/0220200349

Ardhuin, F., Stutzmann, E., Schimmel, M., & Mangeney, A. (2011). Ocean wave sources of seismic noise. Journal of Geophysical Research: Oceans (1978–2012), 116(C9). https://doi.org/10.1029/2011jc006952

Ardhuin, F., Rawat, A., & Aucan, J. (2014). A numerical model for free infragravity waves: Definition and validation at regional and global scales. Ocean Modelling, 77, 20–32. https://doi.org/10.1016/j.ocemod.2014.02.006

Ardhuin, F., Gualtieri, L., & Stutzmann, E. (2015). How ocean waves rock the Earth: Two mechanisms explain microseisms with periods 3 to 300 s. Geophysical Research Letters, 42, 765–772. https://doi.org/10.1002/2014GL062782

Ardhuin, F. (2018). Large Scale Forces Under Surface Gravity Waves at a Wavy Bottom: A Mechanism for the Generation of Primary Microseisms. Geophysical Research Letters, 45(16), 8173–8181. https://doi.org/10.1029/2018gl078855

Aucan, J., & Ardhuin, F. (2013). Infragravity waves in the deep ocean: An upward revision. Geophysical Research Letters, 40(13), 3435–3439. https://doi.org/10.1002/grl.50321

Babcock, J. M., B. A. Kirkendall, and J. A. Orcutt, Relationships between ocean bottom noise and the environment, Bull. Seismol. Soc. Am., 84, 1991 – 2007, 1994.

Barcheck, G., Abers, G. A., Adams, A. N., Bécel, A., Collins, J., Gaherty, J. B., et al. (2020). The Alaska Amphibious Community Seismic Experiment. Seismological Research Letters, 91(6), 3054–3063. https://doi.org/10.1785/0220200189

Bécel, A., Laigle, M., Diaz, J., Montagner, J. -P., & Hirn, A. (2011). Earth's free oscillations recorded by free-fall OBS ocean-bottom seismometers at the Lesser Antilles subduction zone. Geophysical Research Letters, 38(24), n/a-n/a. https://doi.org/10.1029/2011gl049533

Bell, S. W., Forsyth, D. W., & Ruan, Y. (2015). Removing Noise from the Vertical Component Records of Ocean-Bottom Seismometers: Results from Year One of the Cascadia Initiative. Bulletin of the Seismological Society of America, 105(1), 300–313. https://doi.org/10.1785/0120140054

Bendat, J. S., & Piersol, A. G. (2010). Random Data: Analysis and Measurement Procedures (4th ed.). Wiley.

Bird, P. (2003), An updated digital model of plate boundaries, Geochem. Geophys. Geosyst., 4, 1027, doi:10.1029/2001GC000252, 3.

Bodmer, M., Toomey, D. R., Hooft, E. E., Nábělek, J., & Braunmiller, J. (2015). Seismic anisotropy beneath the Juan de Fuca plate system: Evidence for heterogeneous mantle flow. Geology, G37181.1-5. https://doi.org/10.1130/g37181.1

Bodmer, M., Toomey, D. R., Hooft, E. E. E., & Schmandt, B. (2018). Buoyant Asthenosphere Beneath Cascadia Influences Megathrust Segmentation. Geophysical Research Letters, 45(14), 6954–6962. https://doi.org/10.1029/2018gl078700

Bogiatzis, P., Karamitrou, A., Neale, J. W., Harmon, N., Rychert, C. A., & Srokosz, M. (2020). Source Regions of Infragravity Waves Recorded at the Bottom of the Equatorial Atlantic Ocean, Using OBS of the PI-LAB Experiment. Journal of Geophysical Research: Oceans, 125(6). https://doi.org/10.1029/2019jc015430

Bowden, D. C., Kohler, M. D., Tsai, V. C., & Weeraratne, D. S. (2016). Offshore Southern California lithospheric velocity structure from noise cross-correlation functions. Journal of Geophysical Research: Solid Earth. https://doi.org/10.1002/2016jb012919

Bromirski, P. D., Duennebier, F. K., & Stephen, R. A. (2005). Mid-ocean microseisms. Geochemistry, Geophysics, Geosystems, 6(4), n/a-n/a. https://doi.org/10.1029/2004gc000768

Cai, C., Wiens, D. A., Shen, W., & Eimer, M. (2018). Water input into the Mariana subduction zone estimated from ocean-bottom seismic data. Nature Publishing Group, 1–12. https://doi.org/10.1038/s41586-018-0655-4

Carchedi C. J. W., J. B. Gaherty, S. C. Webb, D. J. Shillington; Investigating Short-Period Lake-Generated Microseisms Using a Broadband Array of Onshore and Lake-Bottom Seismometers. Seismological Research Letters 2022; doi: https://doi.org/10.1785/0220210155

Collins, J. A., Vernon, F. L., Orcutt, J. A., Stephen, R. A., Peal, K. R., Wooding, F. B., et al. (2001). Broadband seismology in the oceans: Lessons from the Ocean Seismic Network Pilot

Experiment. Geophysical Research Letters, 28(1), 49–52. https://doi.org/10.1029/2000gl011638

Collins, J. A., Wolfe, C. J., and Laske, G. (2012), Shear wave splitting at the Hawaiian hot spot from the PLUME land and ocean bottom seismometer deployments, Geochem. Geophys. Geosyst., 13, Q02007, doi:10.1029/2011GC003881.

Cox, C., Deaton, T., & Webb, S. (1984). A Deep-Sea Differential Pressure Gauge. Journal of Atmospheric and Oceanic Technology, 1(3), 237–246. https://doi.org/10.1175/1520-0426(1984)001

Crawford, W. C., S.C. Webb, and J. A. Hildebrand, Seafloor compliance observed by long period pressure and displace- ment measurements, J. Geophys. Res., 96, 16,151-16,160, 1991.

Crawford, W. C., & Webb, S. C. (2000). Identifying and Removing Tilt Noise from Low-Frequency (<0.1Hz) Seafloor Vertical Seismic Data. Bulletin of the Seismological Society of America, 952–963.

Crawford, W., Ballu, V., Bertin, X., & Karpytchev, M. (2015). The sources of deep ocean infragravity waves observed in the North Atlantic Ocean. Journal of Geophysical Research: Oceans, 120(7), 5120–5133. https://doi.org/10.1002/2014jc010657

Doran, A. K., & Laske, G. (2016). Infragravity waves and horizontal seafloor compliance. Journal of Geophysical Research: Solid Earth, 121(1), 260–278. https://doi.org/10.1002/2015jb012511

Doran, A. K., & Laske, G. (2017). Ocean-Bottom Seismometer Instrument Orientations via Automated Rayleigh-Wave Arrival-Angle MeasurementsOcean-Bottom Seismometer Instrument Orientations via Automated Rayleigh-Wave Arrival-Angle Measurements. Bulletin of the Seismological Society of America, 107(2), 691–708. https://doi.org/10.1785/0120160165

Doran, A. K., Rapa, M., Laske, G.,Babcock, J., & McPeak, S. (2019).Calibration of differential pressure gauges through in situ testing.Earth and Space Science, 6, https://doi.org/10.1029/2019EA000783

Doran, A. K., & Laske, G. (2019). Seismic Structure of Marine Sediments and Upper Oceanic Crust Surrounding Hawaii. Journal of Geophysical Research: Solid Earth, 124(2), 2038–2056. https://doi.org/10.1029/2018jb016548

Eilon, Z., Abers, G. A., Jin, G., and Gaherty, J. B. (2014), Anisotropy beneath a highly extended continental rift, Geochem. Geophys. Geosyst., 15, 545– 564, doi:10.1002/2013GC005092.

Eilon, Z. C., & Abers, G. A. (2017). High seismic attenuation at a mid-ocean ridge reveals the distribution of deep melt. Science Advances, 3(5), e1602829. https://doi.org/10.1126/sciadv.1602829

Grob, M., A. Maggi, and E. Stutzmann (2011), Observations of the seasonality of the Antarctic microseismic signal, and its association to sea ice variability, Geophys. Res. Lett., 38, L11302,doi:10.1029/2011GL047525

Hasselmann, K. (1963). A statistical analysis of the generation of microseisms. Reviews of Geophysics, 1(2), 177–210. https://doi.org/ 10.1029/RG001i002p00177

Hawley, W. B., Allen, R. M., & Richards, M. A. (2016). Tomography reveals buoyant asthenosphere accumulating beneath the Juan de Fuca plate. Science, 353(6306), 1406–1408. https://doi.org/10.1126/science.aad8104

Hilmo, R., & Wilcock, W. S. D. (2020). Physical Sources of High-Frequency Seismic Noise on Cascadia Initiative Ocean Bottom Seismometers. Geochemistry, Geophysics, Geosystems, 21(10). https://doi.org/10.1029/2020gc009085

International Hydrographic Organization, IHO (1953): Limits of Oceans and Seas. International Hydrographic Organization, Special Publication No 23, 3rd Edition, IMP, Monégasque - Monte-Carlo, 45 pp, hdl:10013/epic.37175.d001

Janiszewski, H. A., & Abers, G. A. (2015). Imaging the Plate Interface in the Cascadia Seismogenic Zone: New Constraints from Offshore Receiver Functions. Seismological Research Letters, 86(5), 1261–1269. https://doi.org/10.1785/0220150104

Janiszewski, H. A., Gaherty, J. B., Abers, G. A., Gao, H., & Eilon, Z. C. (2019). Amphibious surface-wave phase-velocity measurements of the Cascadia subduction zone. Geophysical Journal International, 217(3), 1929–1948. https://doi.org/10.1093/gji/ggz051

Jin, G., Gaherty, J. B., Abers, G. A., Kim, Y., Eilon, Z., & Buck, W. R. (2015). Crust and upper mantle structure associated with extension in the Woodlark Rift, Papua New Guinea from Rayleigh-wave tomography. Geochemistry, Geophysics, Geosystems, 16(11), 3808–3824. https://doi.org/10.1002/2015gc005840

Kohler, M. D., Hafner, K., Park, J., Irving, J. C. E., Caplan-Auerbach, J., Collins, J., et al. (2020). A Plan for a Long-Term, Automated, Broadband Seismic Monitoring Network on the

Global Seafloor. Seismological Research Letters, 91(3), 1343–1355. https://doi.org/10.1785/0220190123

Laske, G., Amanda Markee, John A. Orcutt, Cecily J. Wolfe, John A. Collins, Sean C. Solomon, Robert S. Detrick, David Bercovici, Erik H. Hauri, Asymmetric shallow mantle structure beneath the Hawaiian Swell-evidence from Rayleigh waves recorded by the PLUME network, Geophysical Journal International, Volume 187, Issue 3, December 2011, Pages 1725–1742, https://doi.org/10.1111/j.1365-246X.2011.05238.x

Laurindo, L.C., Mariano, A.J., and Lumpkin, R. (2017). An improved near-surface velocity climatology for the global ocean from drifter observations. Deep Sea Research Part I: Oceanographic Research Papers, 124, 73-92. https://doi.org/10.1016/j.dsr.2017.04.009.

Leahy, G. M., Collins, J. A., Wolfe, C. J., Laske, G., & Solomon, S. C. (2010). Underplating of the Hawaiian Swell: evidence from teleseismic receiver functions. Geophysical Journal International, 183(1), 313–329. https://doi.org/10.1111/j.1365-246x.2010.04720.x

Lee, T. R., Wood, W. T., & Phrampus, B. J. (2018). Global derived datasets for use in k-NN machine learning prediction of global seafloor total organic carbon (Version 1) [Data set]. Zenodo. https://doi.org/10.5281/zenodo.1471639

Lin, PY., Gaherty, J., Jin, G. et al. High-resolution seismic constraints on flow dynamics in the oceanic asthenosphere. Nature 535, 538–541 (2016). https://doi.org/10.1038/nature18012

Lior, I., Sladen, A., Rivet, D., Ampuero, J.P., Hello, Y., Becerril, C., et al. (2021). On the Detection Capabilities of Underwater DAS. Journal of Geophysical Research: Solid Earth, 126, e2020JB020925. https://doi.org/10.1029/2020JB020925

Longuet-Higgins, M. S. (1950), A theory of the origin of microseisms, Philos. Trans. R. Soc., 243, 1–35, doi:10.1098/rsta. 1950.0012.

Lynner, C., & Bodmer, M. (2017). Mantle flow along the eastern North American margin inferred from shear wave splitting. Geology, 1–4. https://doi.org/10.1130/g38980.1

Mark, H. F., Collins, J. A., Lizarralde, D., Hirth, G., Gaherty, J. B., Evans, R. L., & Behn, M. D. (2021). Constraints on the depth, thickness, and strength of the G discontinuity in the central Pacific from S receiver functions. Journal of Geophysical Research: Solid Earth, 126, e2019JB019256. https://doi.org/10.1029/2019JB019256

McNamara, D. E., & Buland, R. P. (2004). Ambient Noise Levels in the Continental United States. Bulletin of the Seismological Society of America, 94(4), 1517–1527. https://doi.org/10.1785/012003001

Montagner, J.-P., Karczewski, J.-F., Romanowicz, B., Bouaricha, S., Lognonne´, P., Roult, G., et al. (1994). The French Pilot Experiment OFM-SISMOBS: first scientific results on noise level and event detection. Physics of the Earth and Planetary Interiors, 84(1–4), 321–336. https://doi.org/10.1016/0031-9201(94)90050-7

Mosher, S. G., Z. C. Eilon, H. A. Janiszewski, P. Audet, Probabilistic Inversion of Seafloor Com- pliance for Oceanic Crustal Shear Velocity Structure Using Mixture Density Neural Networks, in review at JGR: Solid Earth

Müller, R. D., Sdrolias, M., Gaina, C., & Roest, R. W. (2008). Age, spreading rates, and spreading asymmetry of the world's ocean crust. Geochemistry, Geophysics, Geosystems, 9, Q04006. https://doi.org/10.1029/2007GC001743

Pawlowicz, R., 2020. "M_Map: A mapping package for MATLAB", version 1.4m, [Computer software], available online at www.eoas.ubc.ca/~rich/map.html.

Peterson (1993). Observation and modeling of seismic background noise, U.S. Geol. Surv. Tech. Rept. 93-322, 1–95.

Purdy, G. M., and J. A. Orcutt, Broadband seismology in the oceans - Towards a five-year plan, Ocean Seismic Net./Joint Oceanogr. Inst., Washington, D. C., 1995.

Ruan, Y., D. W. Forsyth, and S. W. Bell (2014), Marine sediment shear velocity structure from the ratio of displacement to pressure of Rayleigh waves at seafloor, J. Geophys. Res. Solid Earth, 119, 6357–6371, doi:10.1002/2014JB011162.

Russell, J. B., Gaherty, J. B., Lin, P.-Y. P., Lizarralde, D., Collins, J. A., Hirth, G., & Evans, R. L. (2019). High-resolution constraints on Pacific upper mantle petrofabric inferred from surface-wave anisotropy. Journal of Geophysical Research: Solid Earth, 124, 631– 657. https://doi.org/10.1029/2018JB016598

Rychert, C. A., Harmon, N., & Tharimena, S. (2018). Scattered wave imaging of the oceanic plate in Cascadia. Science Advances, 4(2), eaao1908. https://doi.org/10.1126/sciadv.aao1908

Smalls, P. T., Sohn, R. A., & Collins, J. A. (2019). Lake-Bottom Seismograph Observations of Microseisms in Yellowstone Lake. Seismological Research Letters, 90(3), 1200–1208. https://doi.org/10.1785/0220180242

Sohn, Y., & Rebello, N. S. (2002). Supervised and unsupervised spectral angle classifiers. Photogrammetric engineering and remote sensing, 68(12), 1271-1280.

Spica, Z. J., Nishida, K., Akuhara, T., Pétrélis, F., Shinohara, M., & Yamada, T. (2020). Marine Sediment Characterized by Ocean-Bottom Fiber-Optic Seismology. Geophysical Research Letters, 47(16). https://doi.org/10.1029/2020gl088360

Stephen, R. A., Spiess, F. N., Collins, J. A., Hildebrand, J. A., Orcutt, J. A., Peal, K. R., et al. (2003). Ocean Seismic Network Pilot Experiment. Geochemistry, Geophysics, Geosystems, 4(10). https://doi.org/10.1029/2002gc000485

Stähler, S.C., Sigloch, K., Hosseini, K., Crawford, W.C., Barruol, G., Schmidt-Aursch, M.C., Tsekhmistrenko, M., et al. (2016) Performance report of the RHUM-RUM ocean bottom seismometer network around La Réunion, western Indian Ocean. Adv Geosciences, 41, 43–63. doi:10.5194/adgeo-41-43-2016

Straume, E.O., Gaina, C., Medvedev, S., Hochmuth, K., Gohl, K., Whittaker, J.M., et al. (2019). GlobSed: Updated total sediment thickness in the world's oceans. Geochemistry, Geophysics, Geosystems, 20. DOI: 10.1029/2018GC008115

Sumy, D. F., Lodewyk, J. A., Woodward, R. L., & Evers, B. (2015). Ocean-Bottom Seismograph Performance during the Cascadia Initiative. Seismological Research Letters, 86(5), 1238–1246. https://doi.org/10.1785/0220150110

Tian, Y., & Ritzwoller, M. H. (2017). Improving ambient noise cross-correlations in the noisy ocean bottom environment of the Juan de Fuca plate. Geophysical Journal International, 210(3), 1787–1805. https://doi.org/10.1093/gji/ggx281

Toomey, D., Allen, R., Barclay, A., Bell, S., Bromirski, P., Carlson, R., et al. (2014). The Cascadia Initiative: A Sea Change In Seismological Studies of Subduction Zones. Oceanography, 27(2), 138–150. https://doi.org/10.5670/oceanog.2014.49

Uchiyama, Y., & McWilliams, J. C. (2008). Infragravity waves in the deep ocean: Generation, propagation, and seismic hum excitation. Journal of Geophysical Research: Oceans (1978–2012), 113(C7). https://doi.org/10.1029/2007jc004562

Wan, K. X., Vidavsky, I., & Gross, M. L. (2002). Comparing similar spectra: from similarity index to spectral contrast angle. Journal of the American Society for Mass Spectrometry, 13(1), 85-88. https://doi.org/10.1016/S1044-0305(01)00327-0

Webb, S. C., Zhang, X., & Crawford, W. (1991). Infragravity waves in the deep ocean. Journal of Geophysical Research: Oceans, 96(C2), 2723–2736. https://doi.org/10.1029/90jc02212

Webb, S.C., W. C. Crawford, and J. A. Hildebrand (1994), Long period seismometer deployed at OSN-1, Seismic Waves, 3(1), 4-6,

Webb, S. C. (1998). Broadband seismology and noise under the ocean. Reviews of Geophysics, 36(1), 105–142.

Webb, S. C., & Crawford, W. C. (2010) Shallow-Water Broadband OBS Seismology Bulletin of the Seismological Society of America, 100(4), 1770–1778. https://doi.org/10.1785/0120090203

Weeraratne, D. S., Forsyth, D. W., Yang, Y., and Webb, S. C. (2007), Rayleigh wave tomography beneath intraplate volcanic ridges in the South Pacific, J. Geophys. Res., 112, B06303, doi:10.1029/2006JB004403.

Wei, S. S., Wiens, D. A., Zha, Y., Plank, T., Webb, S. C., Blackman, D. K., et al. (2015). Seismic evidence of effects of water on melt transport in the Lau back-arc mantle. Nature Publishing Group, 518(7539), 395–398. https://doi.org/10.1038/nature14113

Wolfe, C. J., Solomon, S. C., Laske, G., Collins, J. A., Detrick, R. S., Orcutt, J. A., et al. (2009). Mantle Shear-Wave Velocity Structure Beneath the Hawaiian Hot Spot. Science, 326(5958), 1388–1390. https://doi.org/10.1126/science.1180165

Xu, Y., K. D. Koper, and R. Buracu (2017). Lakes as a source of short period (0.5–2 s) microseisms, J. Geophys. Res. 122, 8241–8256.

Yang, Z., Sheehan, A. F., Collins, J. A., & Laske, G. (2012). The character of seafloor ambient noise recorded offshore New Zealand: Results from the MOANA ocean bottom seismic experiment. Geochemistry, Geophysics, Geosystems, 13(10), n/a-n/a. https://doi.org/10.1029/2012gc004201

Yang, X., Luo, Y., Xu, H., & Zhao, K. (2020). Shear wave velocity and radial anisotropy structures beneath the central Pacific from surface wave analysis of OBS records. Earth and Planetary Science Letters, 534, 116086. https://doi.org/10.1016/j.epsl.2020.116086

Zha, Y., Webb, S. C., & Menke, W. (2013). Determining the orientations of ocean bottom seismometers using ambient noise correlation. Geophysical Research Letters, 40(14), 3585–3590. https://doi.org/10.1002/grl.50698

Supplementary material for

Broadband Ocean Bottom Seismometer Noise Properties

Helen A. Janiszewski*[1], Z. Eilon[2], J.B. Russell[3], B. Brunsvik[2], J.B. Gaherty[4], S.G. Mosher[5], W.B. Hawley[6], and S. Coats[1]

1. Department of Earth Sciences, University of Hawaiʻi at Mānoa, Honolulu, HI; 2. Dept. of Earth Science, University of Santa Barbara, Santa Barbara, CA; 3. Dept. of Earth, Environmental and Planetary Sciences, Brown University, Providence, RI; 4. School of Earth & Sustainability, Northern Arizona University, Flagstaff, AZ; 5. Department of Earth and Environmental Sciences, University of Ottawa, Ottawa, Canada; 6. Lamont-Doherty Earth Observatory of Columbia University, Palisades, NY

Contents:

Figure S1: Deployment instrumentation and location histograms.
Figure S2: Deployment environmental properties histograms.
Figure S3: Vertical component noise spectra sorted by experiment.
Figure S4: Horizontal component noise spectra sorted by experiment.
Figure S5: Absolute pressure gauge component noise spectra sorted by experiment.
Figure S6: Differential pressure gauge component noise spectra sorted by experiment.
Figure S7: Corrected vertical component noise spectra sorted by experiment.
Figure S8: Horizontal-pressure coherences as a function of water depth.
Figure S9: Results of spectral angle grouping water-depth grid search.
Figure S10: Example of 3-layer spectral angle results for the vertical component.
Figure S11: Example of 3-layer spectral angle results for the horizontal component.
Figure S12: Example of 3-layer spectral angle results for the vertical corrected component.
Figure S13: Significance tests for spectral angle analysis.
Figure S14: Comparison of lake- and shelf-deployed shallow water vertical spectra.
Table S1: Information about the experiments that were used for our analysis. Includes appropriate citation information for datasets, as well as the network names under which the data is catalogs in the IRIS DMC.
Table S2: Assembled metadata parameter table for all examined instruments. A description of the source of the data, including references, is provided in the main text. This table also indicates if a particular channel was flagged as "good" after quality control procedures, where a value of "1" indicates the spectra was accepted and "0" indicates it was discarded.
Data Access: Calculated noise spectra and cross spectra, and metadata table will be archived at Dryad, doi available upon request, will be made public and included with publication.

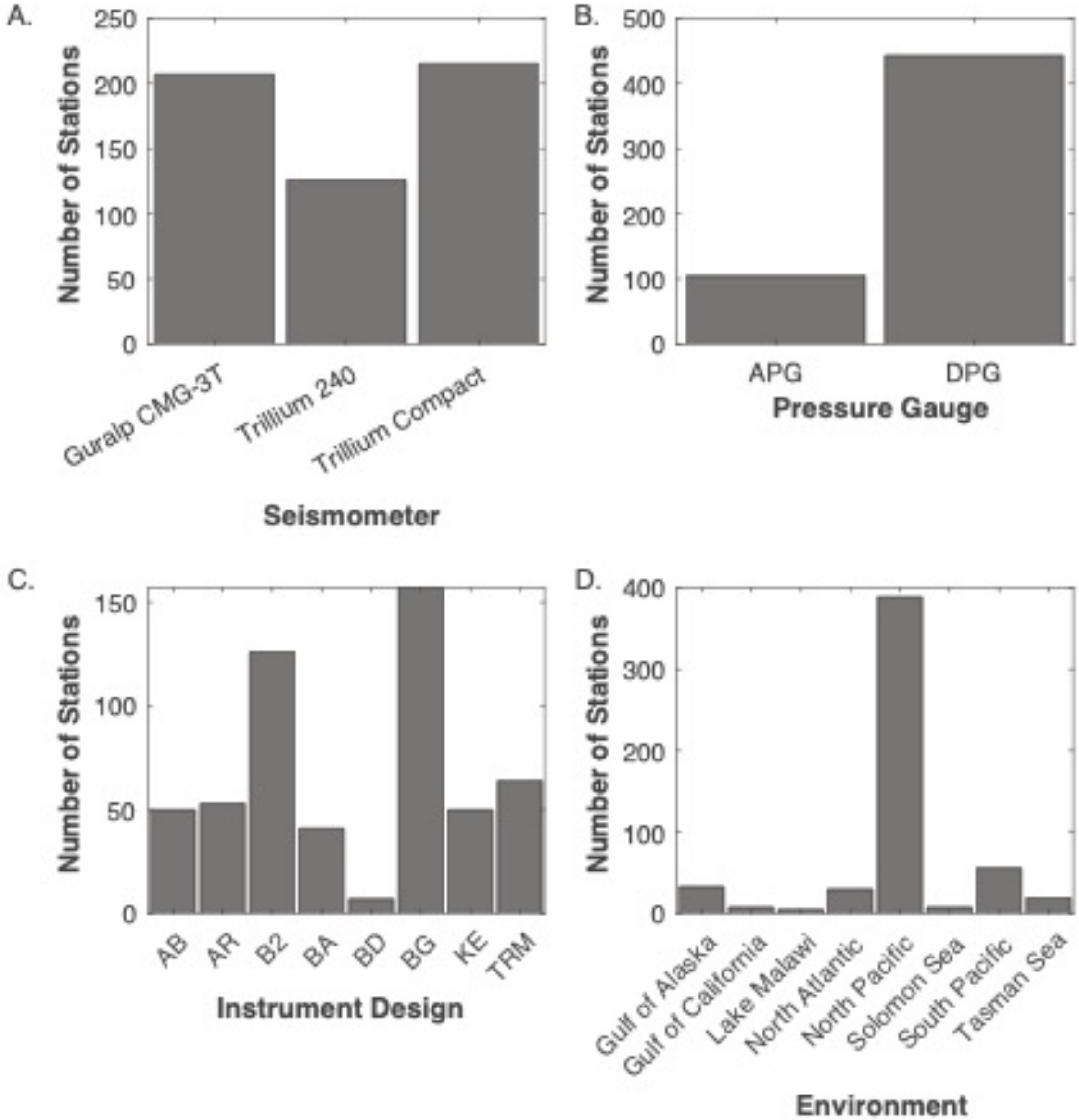

Figure S1: Distributions of categorical station variables. (a) Types of seismometers, (b) types of pressure gauges, (c) BBOBS designs, and (d) deployment environment included in our analysis.

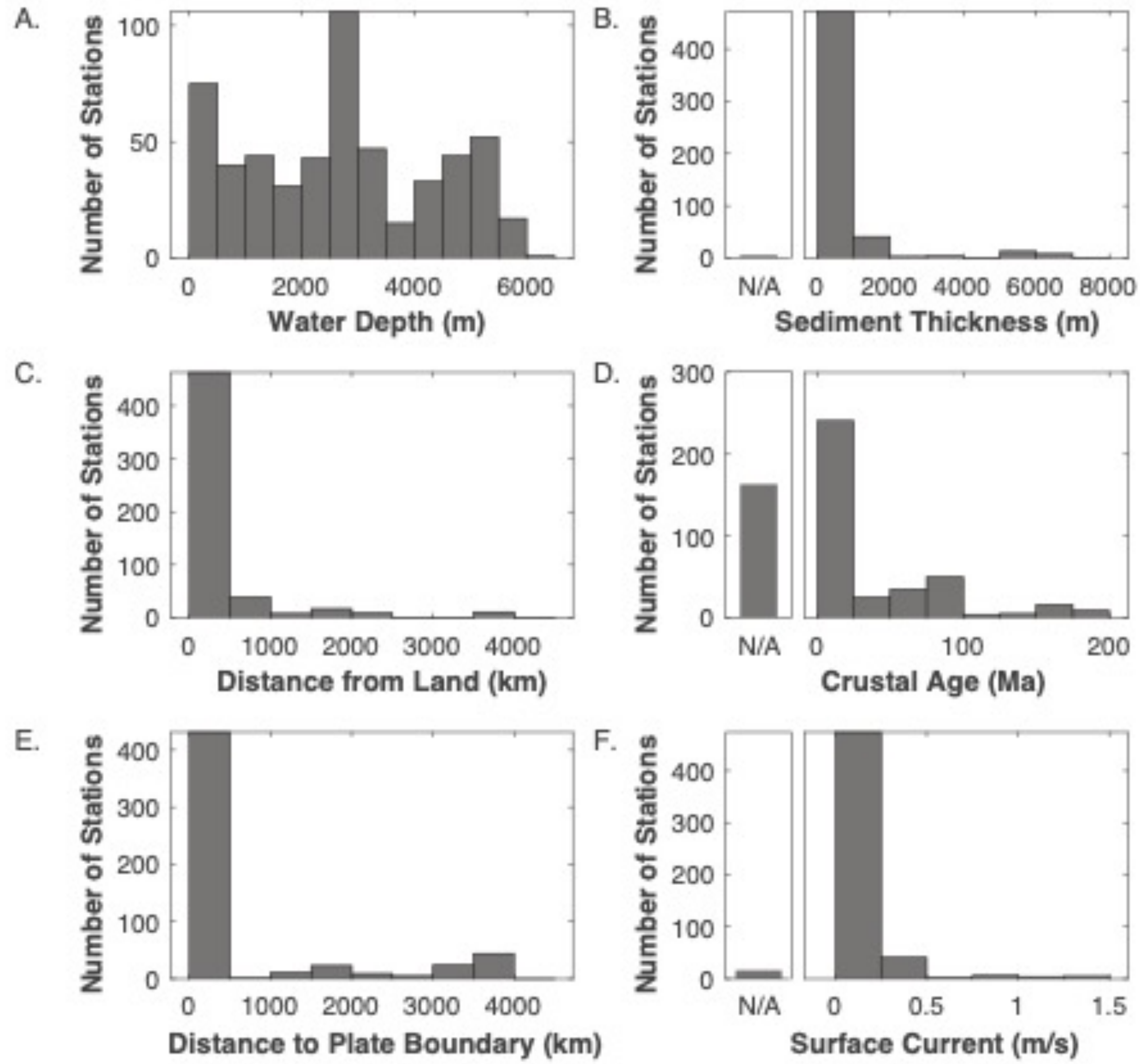

Figure S2: Distributions of numerical station variables. (a) Water depth, (b) sediment thickness, (c) distance from major coastline, (d) crustal age, (e) distance to nearest plate boundary, (f) surface current.

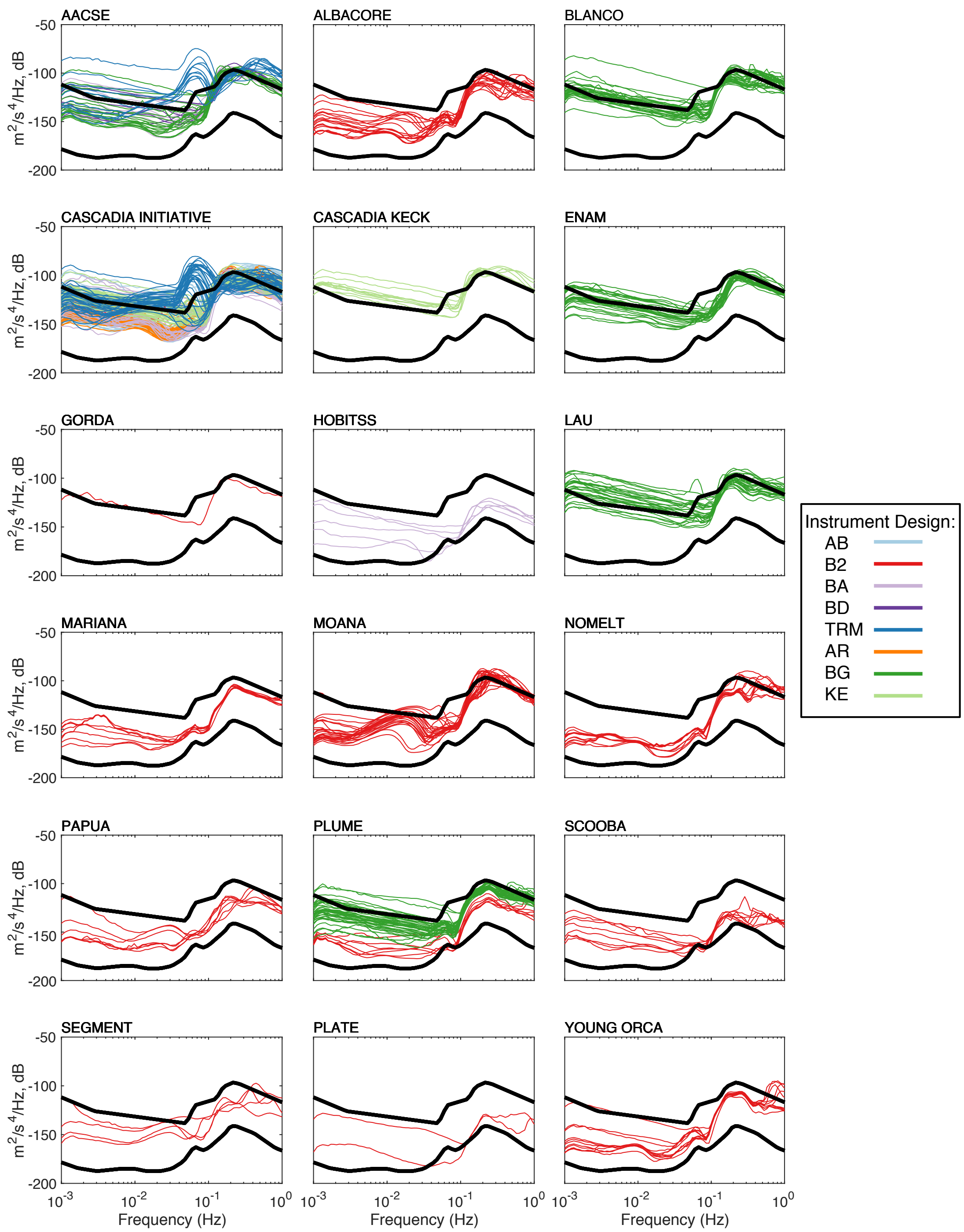

1173

1174 **Figure S3:** Power spectra for the *Z* component for each experiment (Table S1). Spectra are
1175 colored by instrument design; abbreviations are defined in Table 1.

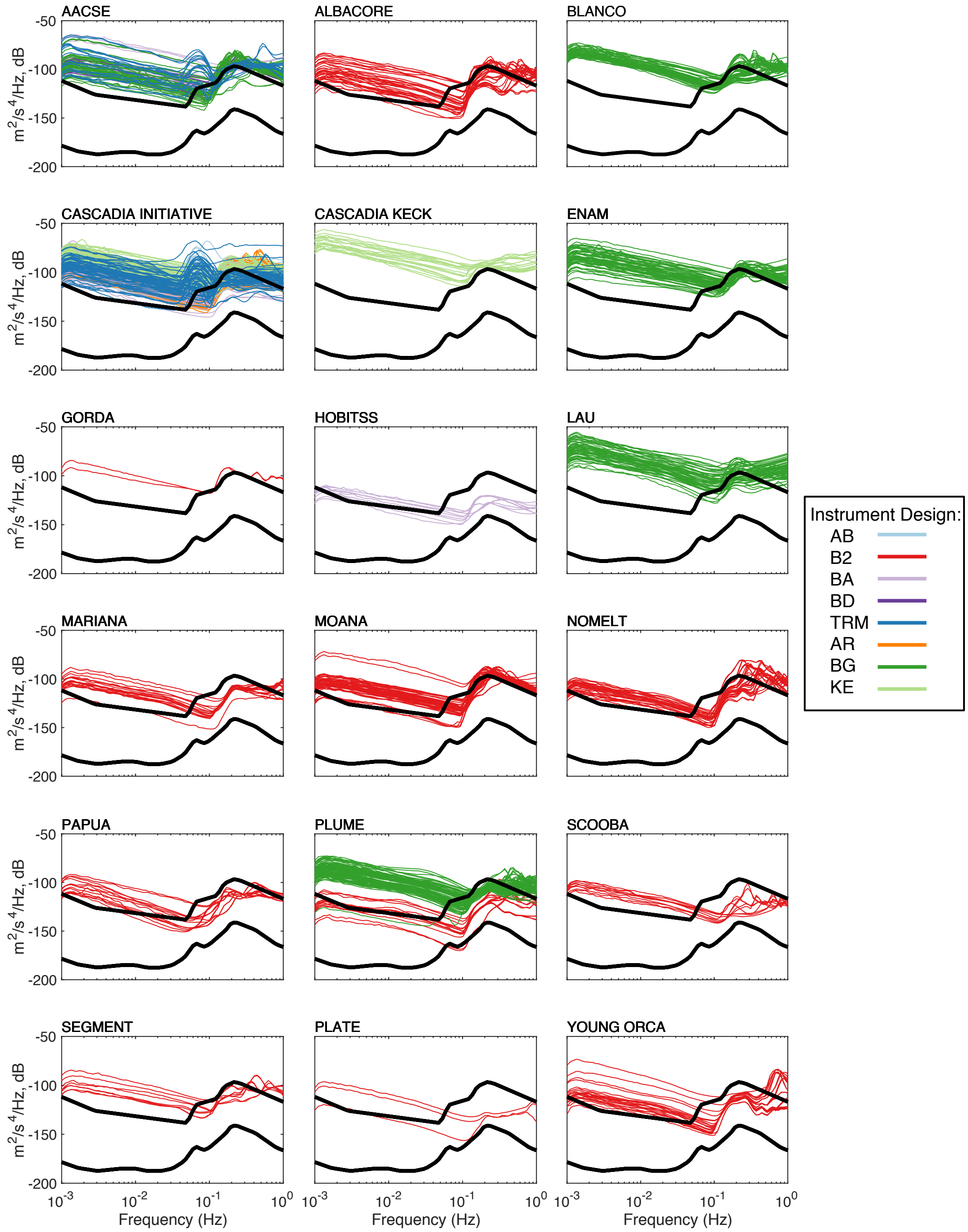

Figure S4: Power spectra for the *H* components for each experiment (Table S1). Spectra are colored by instrument design; abbreviations are defined in Table 1.

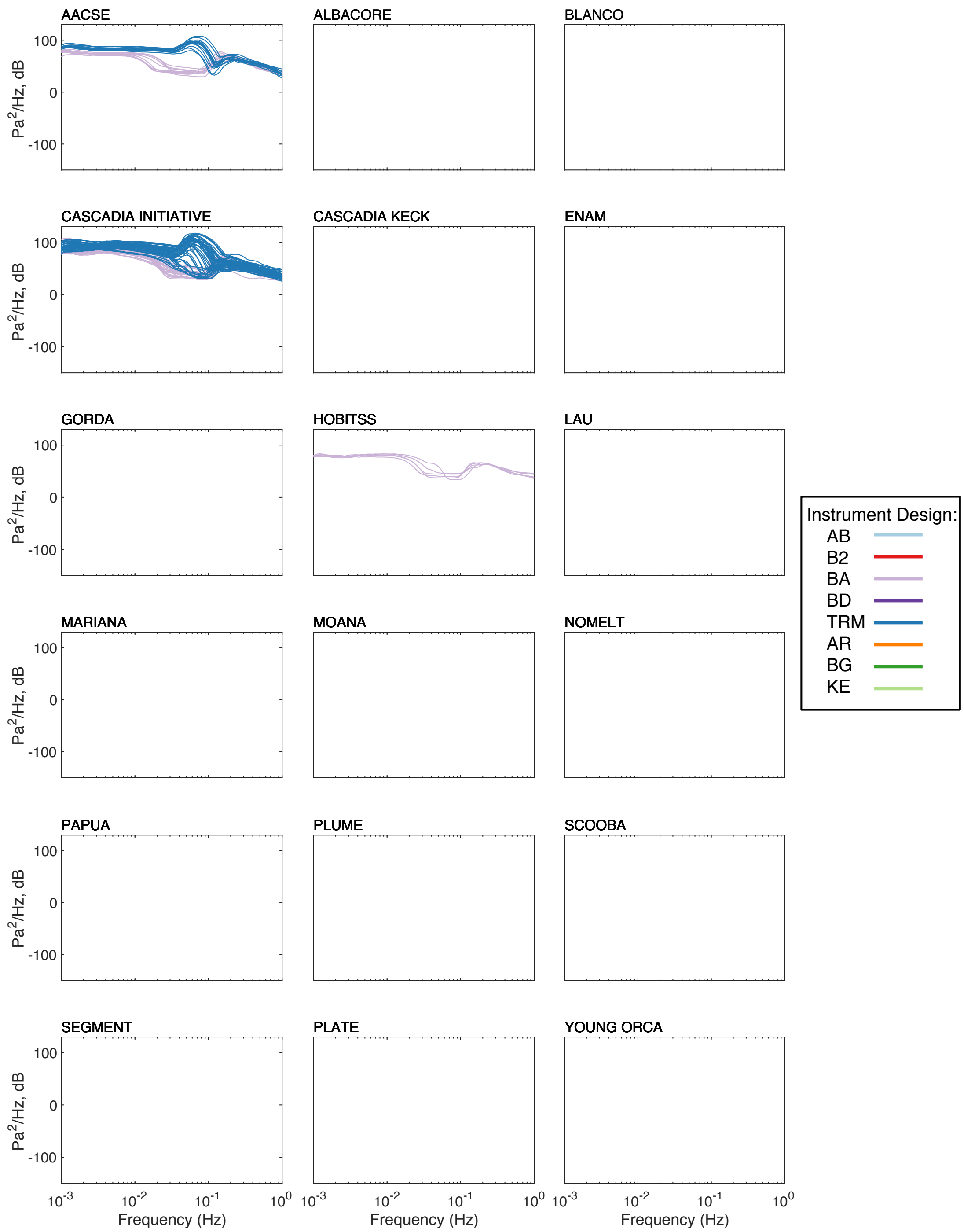

1180

1181 **Figure S5:** Power spectra for the APGs for each experiment (Table S1). Spectra are colored by
1182 instrument design; abbreviations are defined in Table 1. Experiments where APGs were not
1183 deployed do not show any data. The response has not been removed from the instruments.

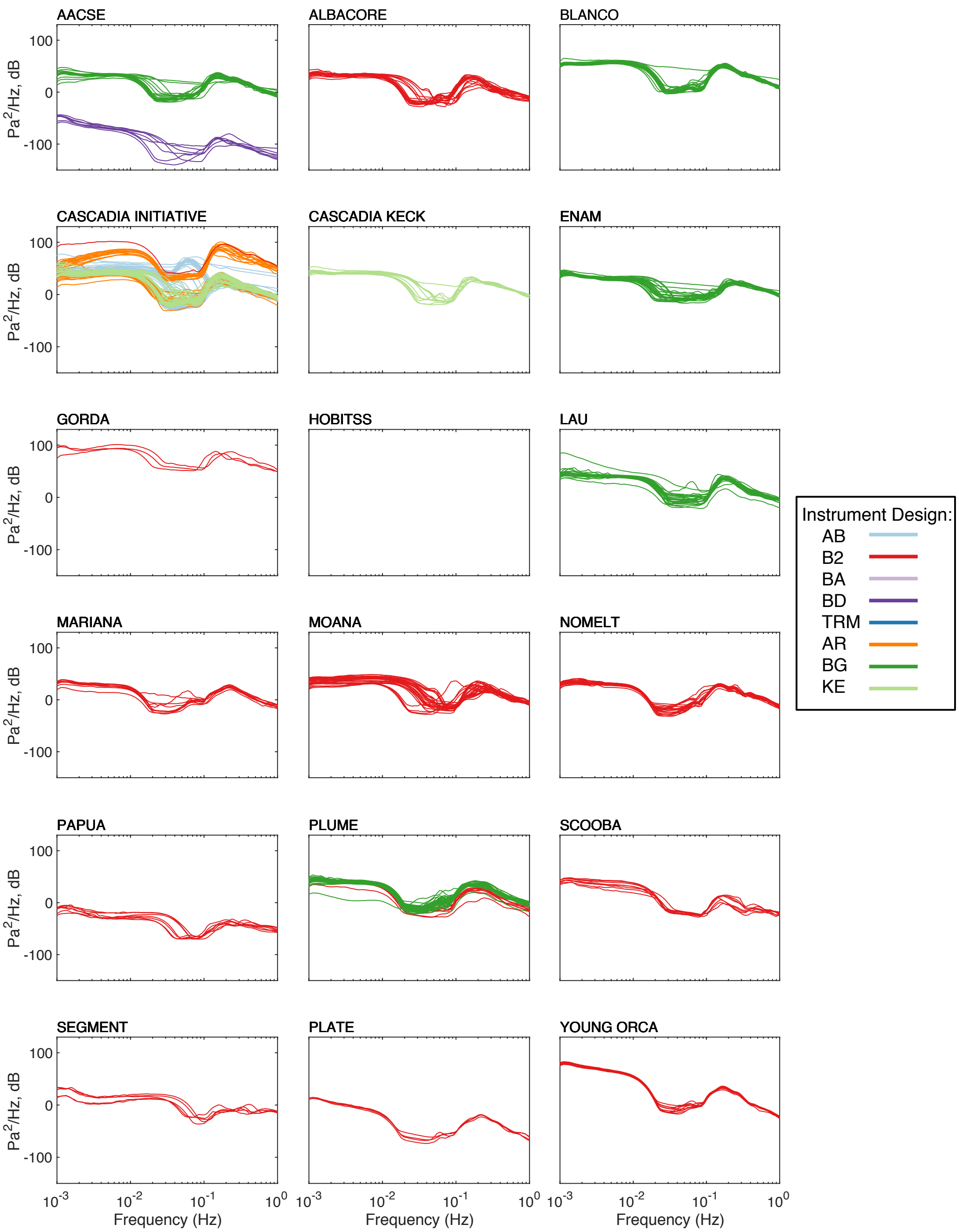

1184

1185 **Figure S6:** Power spectra for the DPGs for each experiment (Table S1). Spectra are colored by
1186 instrument design; abbreviations are defined in Table 1. Response is removed, and data are
1187 processed identically for all experiments. Several of the experiments have instruments or subsets
1188 of instruments where the amplitudes of the DPG spectra are significantly outside the normal
1189 amplitude range. This is likely due to errors in instrument calibration, since it is systematically
1190 observed across different experiment or instrument type subsets.

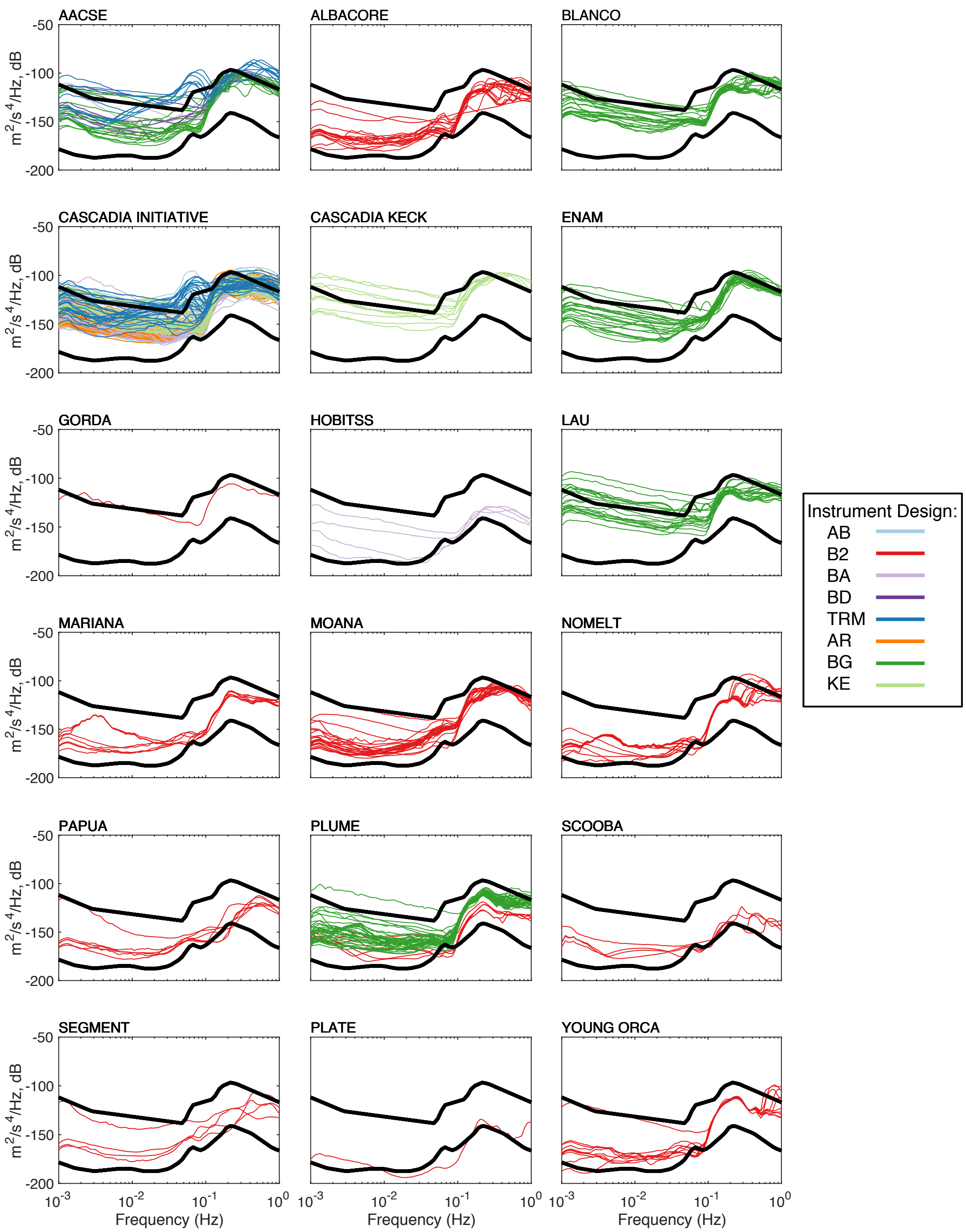

Figure S7: Power spectra for the *Z-corrected* component for each experiment (Table S1). Spectra are colored by instrument design; abbreviations are defined in Table 1.

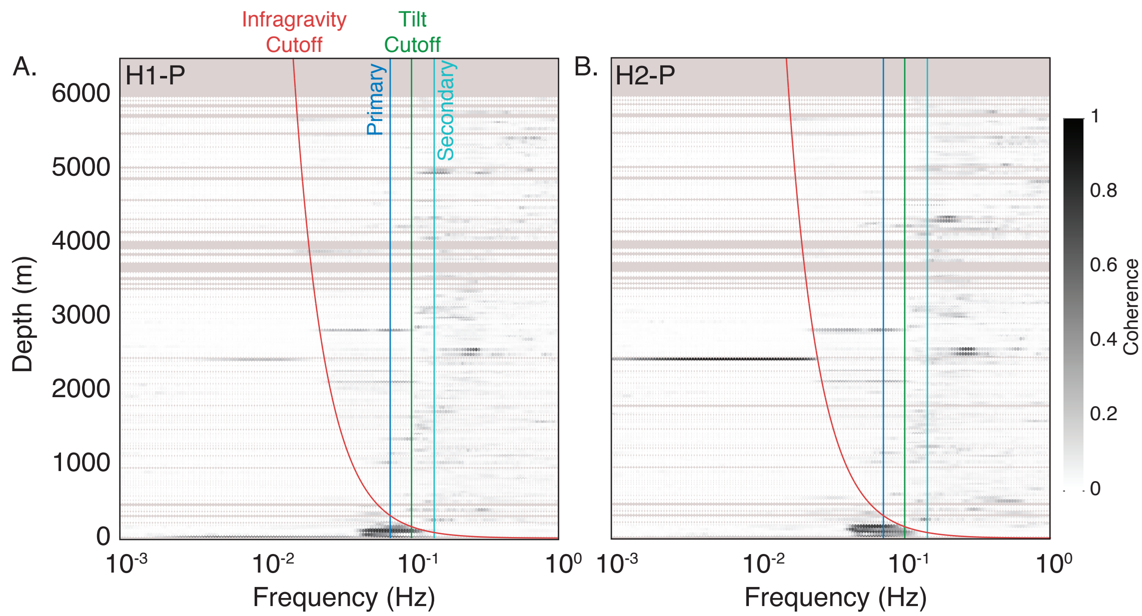

Figure S8: Coherence of the (a) *H1* and (b) *H2* components with the *P* component for each BBOBS compared with the water depth of the instrument. The red line indicates the predicted infragravity cutoff frequency, using $f = \sqrt{\frac{g}{2\pi d}}$ (Bell et al., 2015); the green, dark blue, and light blue lines indicate the tilt cutoff (0.1 Hz), primary (0.07 Hz), and secondary (0.14 Hz) microseism peaks respectively.

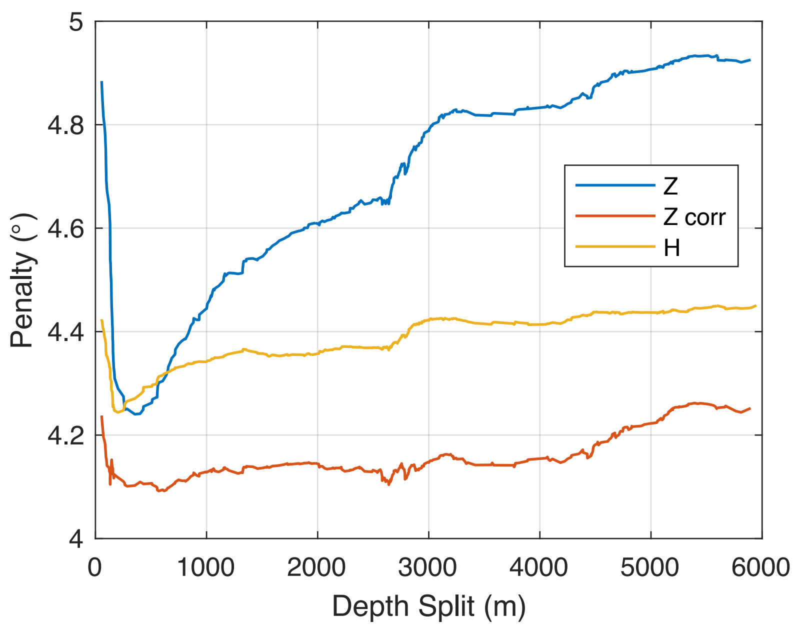

Figure S9: Examples of the grid search procedure used to find the best water depth value to split spectra into two subgroups for the *Z, H,* and *Z-corrected* components. The average penalty is reported as a function of water depth split.

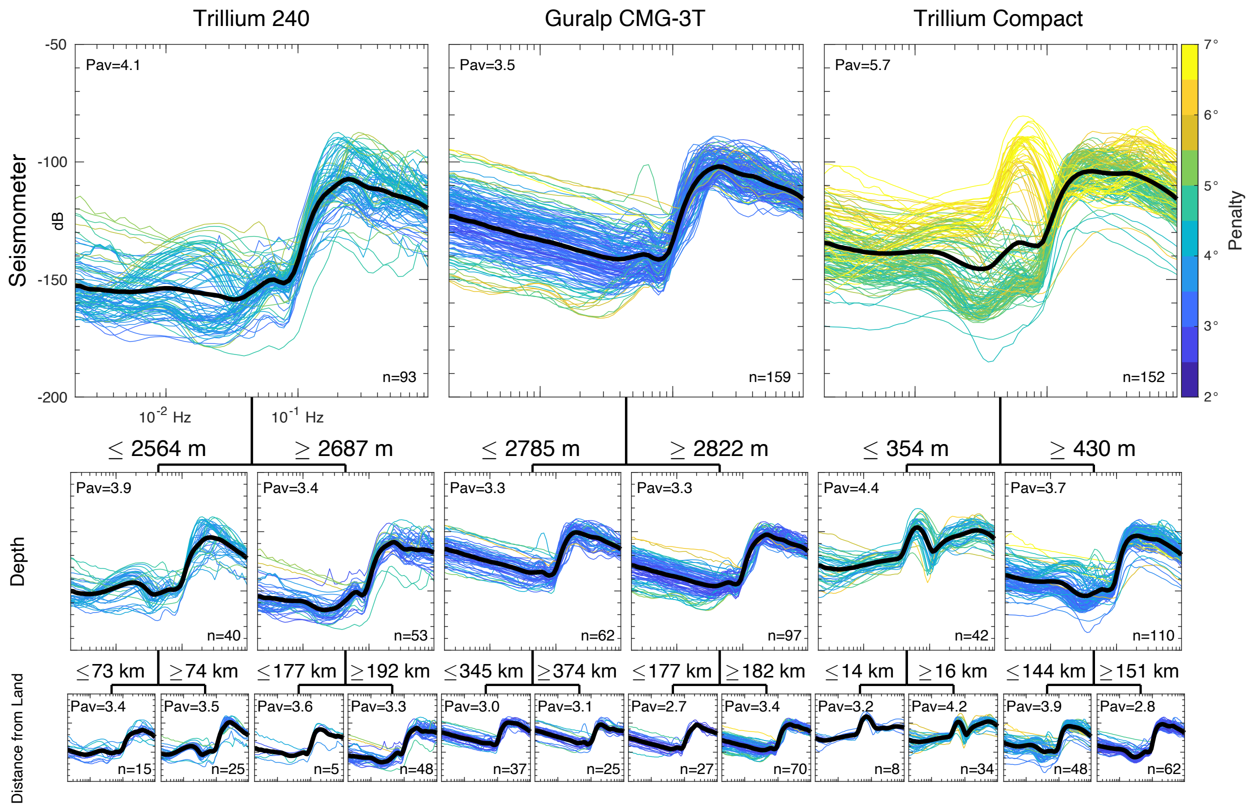

Figure S10: Vertical component 3-layer hierarchy example. Same as Figure 7, but showing an example where the third layer subgroup of spectra is based on "*Distance from Land*" (bottom row).

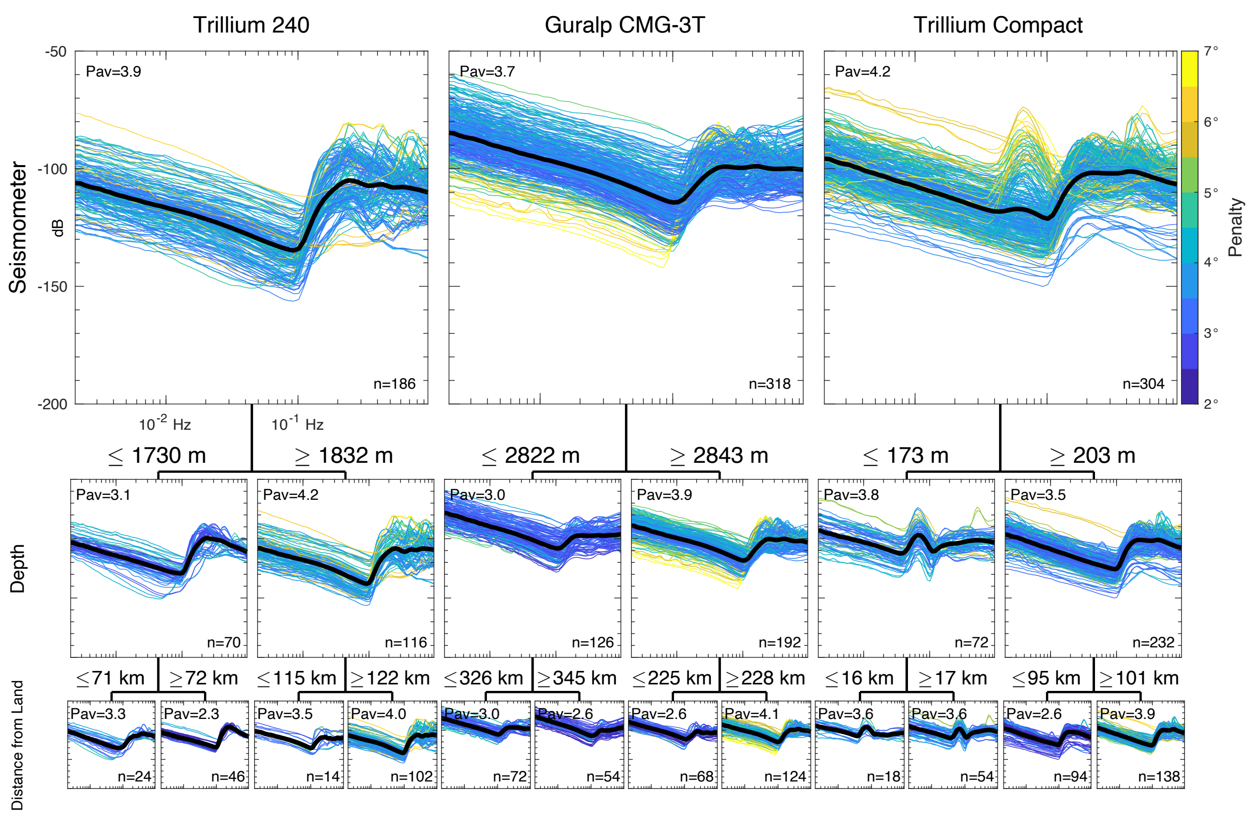

Figure S11: Same as Figure S10, but for the *H* components.

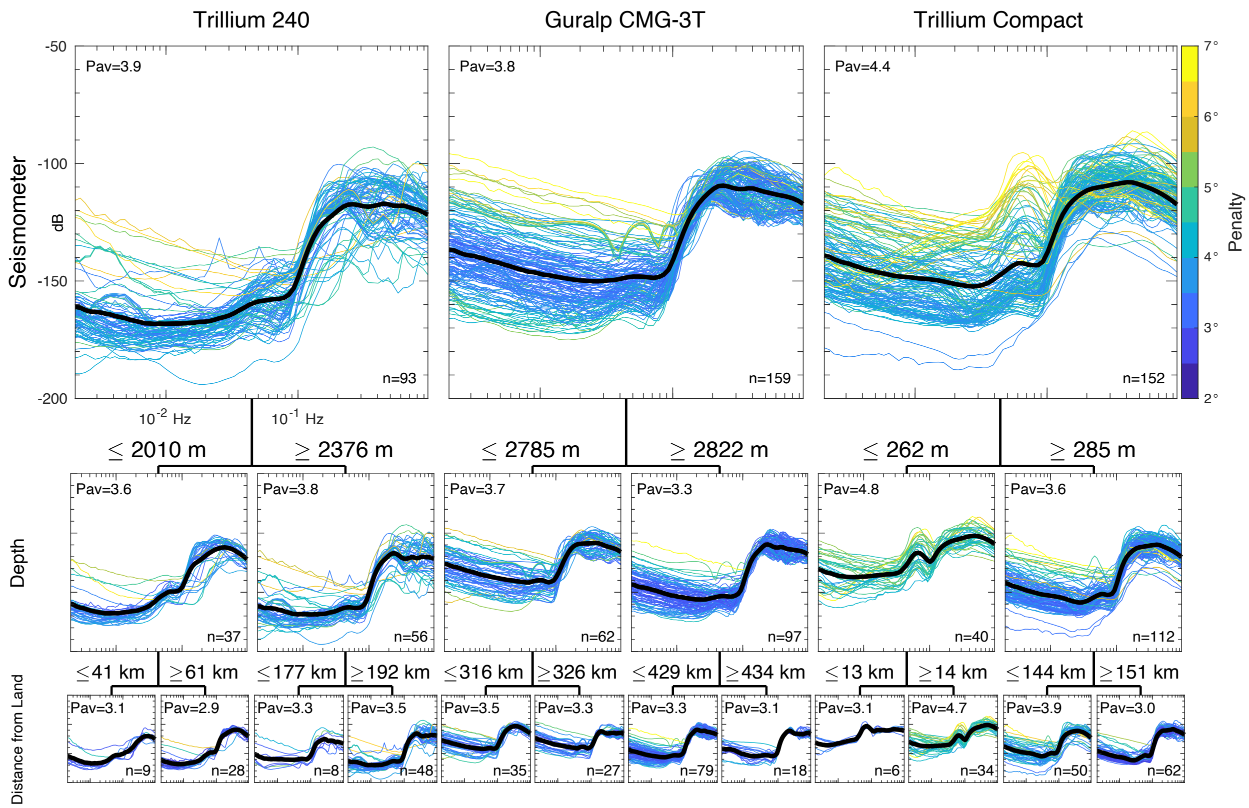

Figure S12: Same as Figure S10, but for the *Z-corrected* component.

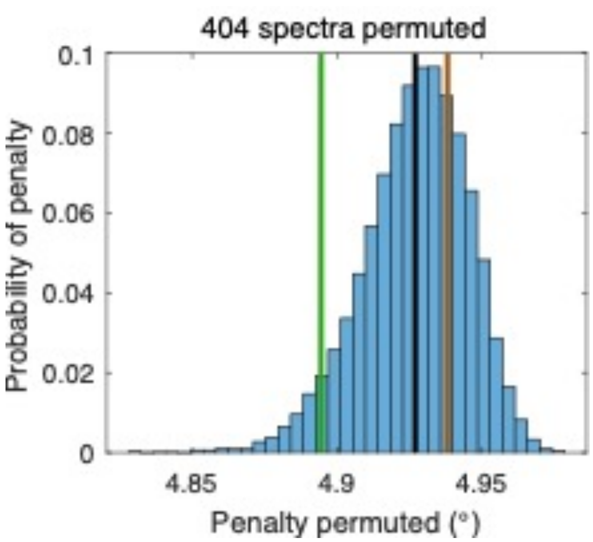

Figure S13: Results of test of distribution of penalties after randomly permuting spectra between clusters for the 3-layer analysis on the *Z* component grouped for *"Seismometer", "Water Depth",* and *"Distance from Land"*. Averaged results of the random permutations (black), compared with the baseline penalty (brown). The green line shows the penalty above which 95% of perturbations resulted in.

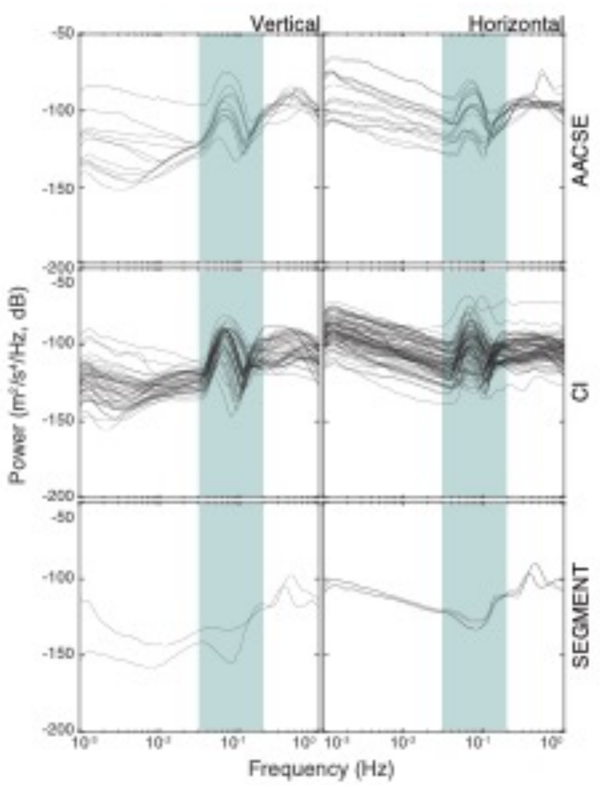

Figure S14: Comparison of vertical and horizontal spectra from all BBOBS deployed in water depths < 500 m, which include instruments from the AACSE, CI, and SEGMeNT experiments (Table S1). Blue shaded region extends over the primary microseism band, and is meant to emphasize the difference in spectra between instruments deployed on the continental shelf (e.g. AACSE and CI) as opposed to in a lake environment (e.g. SEGMeNT).

Table S1- Experiment List

Experiment Name	Network	Instrument Types	Years	Citation
SCOOBA	ZL	B2	2005-06	Sumy et al., 2013
PLUME	YS	BG, B2	2005-07	Wolfe et al., 2009
MOANA	ZU	B2	2009-10	Collins & Sheehan, 2009
PLATE	Z6	B2	2009-10	Takeo et al., 2014
LAU	YL	BG	2009-10	Zha et al., 2014
ALBACORE	2D	B2	2010-11	Lin et al., 2015
CASCADIA KECK	7A	KE	2010-11	Toomey et al., 2014
PAPUA	ZN	B2	2010-11	Abers & Gaherty, 2010
CASCADIA INITIATIVE	7D	TRM, BA, KE, AR, AB	2011-15	Toomey et al., 2014
NOMELT	ZA	B2	2011-12	Lin et al., 2016
MARIANA	XF	B2	2012-13	Wiens, 2012
BLANCO	X9	BG	2012-13	Nabelek & Braunmiller, 2012
GORDA	Z5	B2, AB, BA	2013-15	Nabelek & Braunmiller, 2013
ENAM	YO	BG	2014-15	Gaherty, 2014
HOBITSS	YH	BA	2014-15	Wallace et al., 2014
SEGMeNT	YQ	B2	2015	Gaherty et al., 2013
AACSE	XO	TRM, BA, BD, BG, KE	2018-19	Abers et al., 2018
YOUNG ORCA	XE	B2	2018-19	Eilon et al., 2021

References

Abers G., D. Wiens, S. Schwartz, A. Sheehan, D. Shillington, L. Worthington, P. Shore, E. Rowland, S. Webb, & A. Adams. (2018). AACSE: Alaska Amphibious Community seismic Experiment [Data set]. International Federation of Digital Seismograph Networks. https://doi.org/10.7914/SN/XO_2018

Abers G, & J. Gaherty. (2010). *Papua Peninsula-Woodlark Rift Imaging Experiment* [Data set]. International Federation of Digital Seismograph Networks. https://doi.org/10.7914/SN/ZN_2010

Collins J, A. Sheehan. (2009). Marine Observations of Anisotropy near Aotearoa [Data set]. International Federation of Digital Seismograph Networks. https://doi.org/10.7914/SN/ZU_2009

Eilon Z. C., James B. Gaherty, Lun Zhang, Joshua Russell, Sean McPeak, Joseph Phillips, Donald W. Forsyth, Göran Ekström; The Pacific OBS Research into Convecting Asthenosphere (ORCA) Experiment. *Seismological Research Letters* 2021; doi: https://doi.org/10.1785/0220210173

Gaherty J. (2014). *Eastern North American Margin Community Seismic Experiment* [Data set]. International Federation of Digital Seismograph Networks. https://doi.org/10.7914/SN/YO_2014

Gaherty J, Cindy Ebinger, Andy Nyblade, & Donna Shillington. (2013). *Study of Extension and maGmatism in Malawi aNd Tanzania* [Data set]. International Federation of Digital Seismograph Networks. https://doi.org/10.7914/SN/YQ_2013

Lin, F.-C., M. D. Kohler, P. Lynett, A. Ayca, and D. S. Weeraratne (2015), The 11 March 2011 Tohoku tsunami wavefront mapping across offshore Southern California, J. Geophys. Res. Solid Earth, 120, 3350–3362, doi:10.1002/ 2014JB011524.

Lin, P.-Y.*, J. B. Gaherty, G. Jin, D. Lizarralde, J. A. Collins, R. Evans, and G. Hirth (2016), High-resolution seismic constraints on flow dynamics in the oceanic asthenosphere, *Nature*, 535(7613), 538-541.

Nabelek J, & J Braunmiller. (2012). *Plate Boundary Evolution and Physics at an Oceanic Transform Fault System* [Data set]. International Federation of Digital Seismograph Networks. https://doi.org/10.7914/SN/X9_2012

Nabelek J, & J Braunmiller. (2013). *Seismicity, Structure and Dynamics of the Gorda Deformation Zone* [Data set]. International Federation of Digital Seismograph Networks. https://doi.org/10.7914/SN/Z5_2013

Sumy, D. F., J B. Gaherty, W Y Kim, T Diehl, J A. Collins (2013) The Mechanisms of Earthquakes and Faulting in the Southern Gulf of California. *Bulletin of the Seismological Society of America* 2013;; 103 (1): 487–506. doi: https://doi.org/10.1785/0120120080

Takeo A, D W. Forsyth, D S. Weeraratne, K Nishida, Estimation of azimuthal anisotropy in the NW Pacific from seismic ambient noise in seafloor records, *Geophysical Journal International*, Volume 199, Issue 1, October, 2014, Pages 11–22, https://doi.org/10.1093/gji/ggu240

Toomey, D., Allen, R., Barclay, A., Bell, S., Bromirski, P., Carlson, R., et al. (2014). The Cascadia Initiative: A Sea Change In Seismological Studies of Subduction Zones. Oceanography, 27(2), 138–150. https://doi.org/10.5670/oceanog.2014.49

Wallace L, A Sheehan, S Schwartz, & S Webb. (2014). *Hikurangi Ocean Bottom Investigation of Tremor and Slow Slip* [Data set]. International Federation of Digital Seismograph Networks. https://doi.org/10.7914/SN/YH_2014

Wiens D. (2012). *Mantle serpentinization and water cycling through the Mariana Trench and Forearc* [Data set]. International Federation of Digital Seismograph Networks. https://doi.org/10.7914/SN/XF_2012

Wolfe, C, S. Solomon, G Laske, J Collins, R Detrick, J Orcutt, D Bercovici, E Hauri (2009). Mantle Shear-Wave Velocity Structure Beneath the Hawaiian Hot Spot. Science 326. 1388-90. 10.1126/science.1180165.

Zha, Y., S. C. Webb, S. S. Wei, D. A. Wiens, D. K. Blackman, W. Menke, and J. A. Conder, "Seismological imaging of ridge-arc interaction beneath the Eastern Lau Spreading Center from OBS ambient noise tomography" *Earth and Planetary Science Letters* , v.408 , 2014 , p.194 http://dx.doi.org/10.1016/j.epsl.2014.10.019